



# Cross shelf hydrographic and hydrochemical conditions and their short term variability at the northern Benguela during a normal upwelling season



Volker Mohrholz\*, Anja Eggert, Tim Junker, Günther Nausch, Thomas Ohde, Martin Schmidt

Leibniz-Institute for Baltic Sea Research Warnemünde, Germany

## ARTICLE INFO

### Article history:

Received 3 December 2013

Received in revised form 28 April 2014

Accepted 29 April 2014

Available online 6 May 2014

### Keywords:

Northern Benguela

Coastal upwelling

Wind stress curl

Hydrography

Hydrochemistry

Pseudo-age

Temporal and spatial variability

## ABSTRACT

Cross shelf hydrographic and hydrochemical conditions were investigated during the seasonal maximum of upwelling in the northern Benguela upwelling system. The study combines in situ observations, remotely sensed data and results of a regional 3-dimensional numerical model. In situ observations were recorded along a cross shelf transect off Namibia starting at 20°S 13°E, repeated five times during 16 August 2011 until 19 September 2011. Comparison of wind forcing and sea surface temperatures during the time of the expedition with long-term climatological data as well as the index of intensity of the Benguela upwelling indicates “normal” upwelling conditions in austral winter 2011 in the northern Benguela. Small scale temporal (days) and spatial (km) variability is high during the upwelling season, primarily caused by highly variable wind forcing and dynamics of mesoscale structures like eddies and filaments as found in remotely sensed data. This mesoscale dynamics impact the applicability of a conceptual 2-dimensional circulation model, i.e. a linear succession along the cross-shelf transect. Therefore, an age proxy for surface water was constructed based on oxygen and heat fluxes during the first aging period and on salinity and heat fluxes during the second phase. The application of an age proxy instead of distance to shore successfully validates the succession concept. Furthermore, the investigation of the upwelling strengths by analytical and circulation models verified their dependence on coastal- and curl driven upwelling processes with the onshore dominance of coastal upwelling. In the investigated time period, offshore, curl driven upwelling dominated with a maximum located on the shelf.

© 2014 The Authors. Published by Elsevier B.V. This is an open access article under the CC BY-NC-SA license (<http://creativecommons.org/licenses/by-nc-sa/3.0/>).

## 1. Introduction

Wind forced upwelling is one of the most important processes to connect the deep ocean with the euphotic layer and plays an important role in the global cycle of carbon and nutrients (Ianson and Allen, 2002; Muller-Karger et al., 2005). Although upwelling systems cover only a small fraction of the ocean surface they contribute disproportionately to the global primary production and host many of the major commercially used fish stocks (FAO, 2012). The Benguela upwelling system is one of the large Eastern Boundary upwelling systems (EBUS) that are associated with the highest primary production in the world ocean (e.g. Carr, 2002; Carr and Kearns, 2003). The productivity of Eastern Boundary upwelling systems responds sensitively to changes in physical forcing caused by climate variability (Bakun, 1990; Bakun et al., 2010). Thus,

understanding ecosystem functioning in upwelling areas is of overall interest for managing and protecting these valuable marine areas.

Upwelling of nutrients into the euphotic zone is the initial process of the trophic chain in upwelling systems. Upward directed vertical movement at the base of the surface layer ( $H_{mix}$ ) brings nutrient-rich water into contact with the sea surface, where this water and the dissolved nutrients become part of the actively mixing surface layer. As such, the nutrient supply to the surface layer is a result of the combined action of a vertical upwelling movement of water masses and mixing. Vertical velocity at the base of the surface layer corresponds to a divergence of the horizontal transport within this layer. There are two mechanisms to generate this divergence (Fennel and Lass, 2007). The first is related to the existence of a coast as a natural physical boundary for the cross shore surface transport. Coastal upwelling is governed by the along-shore wind stress near the coast. It is confined to a coastal band with a width of a baroclinic Rossby radius (Charney, 1955; Yoshida, 1955; Fennel, 1999). Coastal upwelling is affected by Kelvin waves that leave a steady state in their wake and reduce the upwelling. Moreover they export the upwelling signal poleward. In the inviscid case, i.e. when frictional effects are neglected, the upwelling ceases completely after the arrival of the Kelvin waves. Therefore only temporal variations of

\* Corresponding author.

E-mail addresses: [Volker.Mohrholz@io-warnemuende.de](mailto:Volker.Mohrholz@io-warnemuende.de) (V. Mohrholz), [Anja.Eggert@io-warnemuende.de](mailto:Anja.Eggert@io-warnemuende.de) (A. Eggert), [Tim.Junker@io-warnemuende.de](mailto:Tim.Junker@io-warnemuende.de) (T. Junker), [Guenther.Nausch@io-warnemuende.de](mailto:Guenther.Nausch@io-warnemuende.de) (G. Nausch), [Thomas.Ohde@io-warnemuende.de](mailto:Thomas.Ohde@io-warnemuende.de) (T. Ohde), [Martin.Schmidt@io-warnemuende.de](mailto:Martin.Schmidt@io-warnemuende.de) (M. Schmidt).

the wind field can excite new upwelling events (Fennel, 1999). The second upwelling mechanism is Ekman pumping, where the vertical velocity  $w$  at the bottom of the mixed layer ( $H_{\text{mix}}$ ) depends on the curl of the local wind stress  $\tau$ :

$$w|_{z=H_{\text{mix}}} = \frac{\text{curl } \tau_z}{\rho f} \quad \text{with } \text{curl } \tau_z = \left( \frac{\partial \tau^{(y)}}{\partial x} - \frac{\partial \tau^{(x)}}{\partial y} \right) \quad (1)$$

where  $\rho$  is the water density, and  $f$  is the Coriolis parameter. Contrary to the Ekman divergence driven upwelling, wind stress curl driven upwelling is not affected by Kelvin waves (Fennel, 1999). This fact illustrates the importance of wind stress curl in upwelling systems since this mechanism is able to maintain upwelling independent of Kelvin waves.

The importance of both upwelling processes for marine systems has been extensively discussed in the recent years (Fennel, 1999; Fennel and Lass, 2007; Jin et al., 2009; Renault et al., 2009; Albert et al., 2010; Veitch et al., 2010). Pickett and Paduan (2003) estimated upwelling due to Ekman transport and pumping in the California current system. Their results suggest that Ekman pumping is nearly as important as upwelling driven by the alongshore winds. However, there exists no estimation on the vertical velocity related to both upwelling mechanisms in the Benguela system so far.

Rykaczewski and Checkley (2008) have shown that the vertical upwelling velocity plays an important role in the size distribution of phytoplankton and in the availability of suitable food for higher trophic levels. Curl driven upwelling favors the smaller phytoplankton species, which are the preferred food for small pelagic fish.

In this paper the results of a field study are presented, that is focused on cross shelf matter transports and plankton succession in the upwelled water along its pathway from the coast towards the open ocean. The experiment was carried out in the northern Benguela upwelling system (BUS) during the seasonal maximum of wind forcing. The BUS off southwestern Africa is one of the four major upwelling systems in the world oceans (Carr and Kearns, 2003; Chavez and Messié, 2009). The BUS consists of a northern and a southern part, separated by the Lüderitz upwelling cell at 27°S (Duncombe Rae, 2005). Both systems are closely connected, but behave differently with respect to wind forcing, seasonality of upwelling, ventilation of the shelf area, and many other aspects (Cury and Shannon, 2004). The northern boundary of the BUS is formed by the Angola Benguela frontal zone (ABFZ) at approximately 15°S to 17°S (Shannon et al., 1987). The southern boundary of the BUS is the Agulhas retroflection zone near the Cape of Good Hope. In the northern BUS the wind forcing has a strong seasonal cycle. Winds are strongest during austral winter months – July, August, and September. During summer (December to March) the trade winds relax. Due to the spatial structure of the wind field the wind stress curl driven vertical current component is positive (upward directed) in a 200 to 300 km wide band along the entire Namibian coast (Bakun and Nelson, 1991; Lass and Mohrholz, 2008; Risien and Chelton, 2008; Fennel et al., 2012).

The amount of nutrients lifted into the euphotic layer depends on both the upwelling intensity and the nutrient content of the source water mass, usually from the central water layer. The northern BUS is the transition area between two different central water masses of the south Atlantic (Duncombe Rae, 2005; Mohrholz et al., 2008), the South Atlantic Central Water (SACW) and the Eastern South Atlantic Central Water (ESACW). Both water masses have different nutrient and dissolved oxygen content. In the Angola Gyre the properties of SACW are modified before it is transported poleward into the BUS by the Angola current and its extension the poleward undercurrent. SACW is nutrient enriched, but oxygen depleted. ESACW originates from the Cape Basin and is well ventilated, but contains less nutrients than the SACW (Mohrholz et al., 2008). ESACW is the dominant water mass in the BUS during the main upwelling season in austral winter, whereas in summer SACW spreads southward up to the Lüderitz

upwelling cell. The seasonal change in central water mass distribution at the Namibian shelf is controlled both by the seasonal variation of trade winds off Namibia and by remote forcing from the equatorial Atlantic (Lass and Mohrholz, 2008).

The main processes in upwelling ecosystems are often treated in frame of 2-dimensional conceptual models of cross shelf circulation and plankton succession. The cross shelf circulation consists of an offshore transport in the surface layer, maintained by Ekman transport and mesoscale dynamics (Kostianoy and Zatsepin, 1996), and an onshore directed compensation flow below the mixed layer. Biological production, biogeochemical processes and fluxes through the boundaries change the properties of upwelled water along the pathway towards the open ocean.

Following the 2-dimensional approach, in situ observations were carried out along a cross shelf transect in the northern Benguela at approximately 20°S, referred to as the SUCCESSION transect. This specific region is often depicted as the northern Namibian cell (e.g. Hardman-Mountford et al., 2003) and was selected since there the alongshore variability of wind forcing and shelf bathymetry is weak. Thus, it is assumed that cross shelf processes dominate the observed structures. In reality the wind driven surface circulation is three dimensional. It also consists of longshore currents and is overlaid with advection components of mesoscale dynamics (filaments, eddies, etc.). Mesoscale dynamics contributes significantly to the offshore export of nutrients (Gruber et al., 2011; Gutknecht et al., 2013). However, on average the upwelled water spreads towards the northwest. Therefore, the measurements along the cross shelf transect represent a projection of the real advection onto the transect. In a simplified view cross shelf matter transports and plankton succession can be described using the distance to the coast as a measure of water mass age. Water masses are younger close to the coast and older further offshore, but this simple concept is impacted by mesoscale structures, like eddies and filaments. The mesoscale dynamics complicate the investigation of both temporal and spatial succession of the plankton community and biogeochemical conditions along the cross-shelf transect because, among others, they depend on the water age. To overcome this problem an age proxy for surface water was constructed based on oxygen and heat fluxes during the first aging period and on salinity and heat fluxes during the second phase. By applying the age proxy instead of distance to shore, the measurements of the interdisciplinary data were successfully rearranged to study the succession of different processes.

This paper deals with the analysis of wind forcing, hydrographic and hydrochemical conditions and the impact of mesoscale dynamics during the annual maximum of upwelling in the northern Benguela. It supplies the basis data and background information for the detailed and specialized investigations of various trophic levels carried out in the interdisciplinary field experiment “SUCCESSION”.

## 2. Material and methods

The used data set consists of in situ measurements carried out during the cruises MSM18/4 and MSM18/5 with the R/V Maria S. Merian, remote sensing data, and results of a regional 3-dimensional coupled hydrodynamic–biogeochemical model of the Benguela upwelling system (Herzfeld et al., 2011; Schmidt and Eggert, 2012).

In situ sampling of hydrographic and hydrochemical parameters was carried out along the SUCCESSION transect across the northern Namibian shelf between approximately 20°S and 22°S (Fig. 1). The transect was directed perpendicular to the coast and covers the shelf, the shelf break, the continental slope and partly the continental rise. At this latitude the bottom topography depicts a double shelf break at 200 m and at 400 m depth, with coastal distances of 60 km and 110 km respectively. In this paper we use the term “shelf” for the entire area within 400 m water depth. The continental slope extends offshore to 250 km distance from the coast. Between 16th August and 19th September 2011 the transect was worked five times to obtain information about the variability of

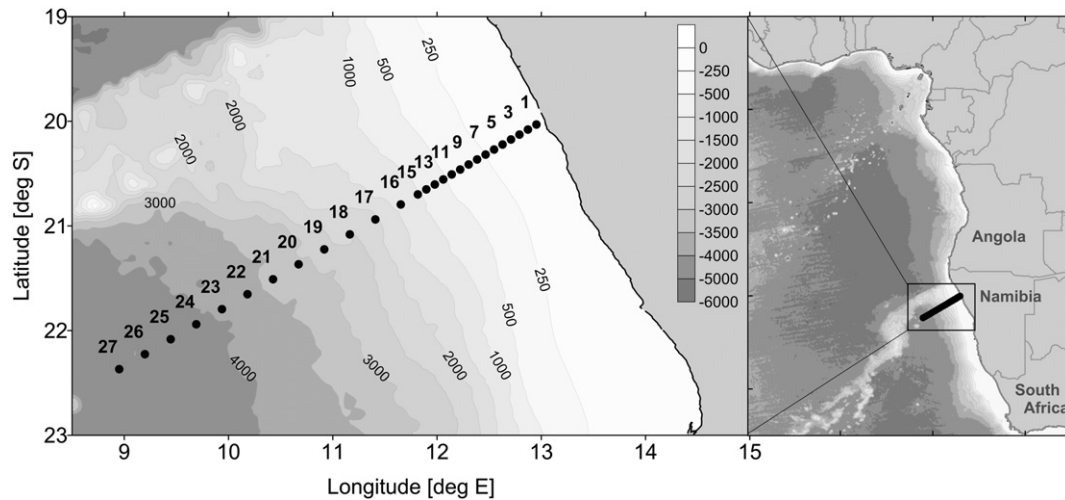


Fig. 1. Position of the SUCESSION transect off the northern Namibian coast. Stations are indicated by black dots. Moorings were deployed at stations 6 and 11.

the main hydrographic parameters at the time scale of mesoscale dynamics, which is about 5 to 30 days. Measurements during the first four legs cover the stations at the shelf and the continental slope from 10 to 230 km distance to the coast (stations 1–18). The fifth run was extended to 500 km offshore. The station distance was 10 NM over the inner shelf (10–50 km distance to the coast) and increases to 30 NM between the westernmost stations. The station distance approximately compares with the internal Rossby radius, which increases from 15 km on the shelf to about 50 km at the offshore limit of the transect. Thus, the larger patterns of mesoscale dynamics are resolved by the station grid. An impression of station grid scaling in relation to surface

expressions of mesoscale patterns can be obtained from Fig. 2. In addition to the data presented in this paper several biochemical and biological parameters were measured to obtain as much information as possible for an integrated view onto the ecosystem.

### 2.1. Wind forcing

Time series of wind speed and wind direction were measured with the ship weather station onboard the R/V Maria S. Merian during the cruise. The raw sampling interval of wind data was 10 s. Data were processed, i.e. inspected for outliers and averaged over 30 min.

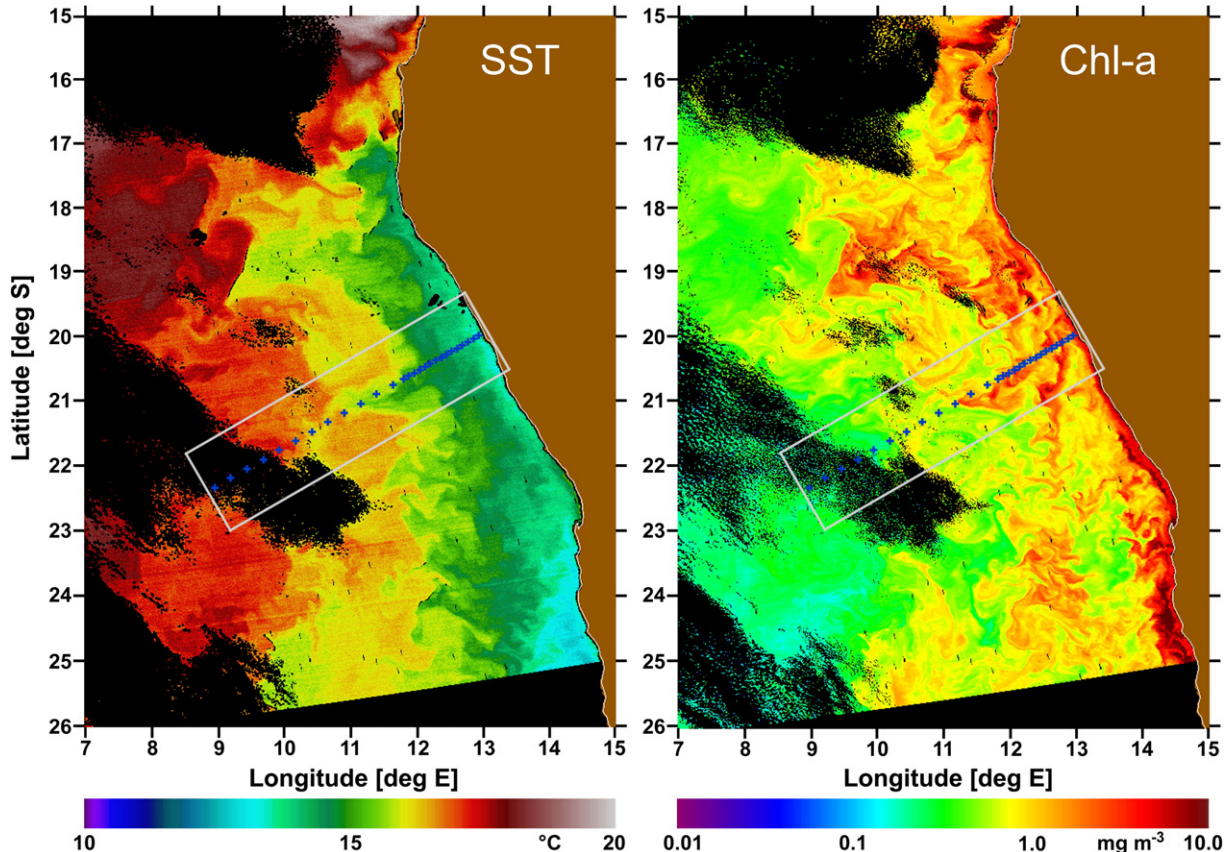


Fig. 2. Sea surface temperature (left) and Chl-a concentration (right) in the beginning of field observations on 24th August 2011 (MODIS Aqua). The crosses depict the stations along the hydrographic transect. The box indicates the detail area of the SUCESSION transect used in Fig. 8.

Additionally, the data were corrected from the mounting height (29 m) of the sensor at the ship to the wind speed at height 10 m using the MATLAB Air–Sea–Toolbox following Large and Pond (1981).

Spatially gridded, daily-averaged wind fields (wind speed, eastward wind, westward wind, northward wind stress) (DASCAT) based on ASCAT (Advanced Scatterometer) data for the period from 21st August until 20th September 2011 were analyzed, except for 17th September 2011, where no data were available (data source: <ftp://ftp.ifremer.fr/ifremer/cersat/products/gridded/MWF/L3/ASCAT/Daily/>). The gridded data have a spatial resolution of 0.25° and are daily composites of 3-day measurements. DASCAT data have been validated with buoy arrays (Bentamy and Fillon, 2011). The difference of the root mean square (RMS) between buoy arrays and DASCAT data was less than 1.7 m s<sup>-1</sup> for wind speed and less than 18° for wind direction.

The DASCAT wind field data of the cruise period were compared to the Scattered Climatology of Ocean Winds (SCOW), which is a climatology of remotely sensed wind based on the QuikSCAT (Quick Scatterometer) measurements during the period of September 1999 to October 2009 (Risien and Chelton, 2008).

## 2.2. Sea surface temperature and chlorophyll

Remotely sensed daily sea surface temperatures (SSTs) and chlorophyll-a (Chl-a) concentrations were used for the characterization of near surface water masses along the cross-shelf transects as well as for the evaluation of their temporal and spatial variability during the field campaign. They were obtained from MODIS (Moderate Resolution Imaging Spectroradiometer) Aqua and Terra level-2 products (data source: <http://oceancolor.gsfc.nasa.gov/>, Feldman and McClain, 2012). The data have a spatial resolution of 1 km. In addition, a monthly level-3 product with 4 km resolution based on the 11 μm SST (data source: <http://disc.sci.gsfc.nasa.gov/giovanni>) was used to discuss the seasonal cycle of SST pattern.

The MODIS Chl-a concentrations were compared with measurements recorded along the cross shelf transect (Hansen et al., 2014–in this issue). This investigation delivered underestimations up to about 60% (N = 42, R<sup>2</sup> = 0.79, RMS = 0.4 mg m<sup>-3</sup>). Uncertainties in the same order of magnitude were also verified in relation to the database of SeaBASS (bio-optical archive and storage system, <http://seabass.gsfc.nasa.gov/>). Dogliotti et al. (2009) and Mendonca et al. (2010) confirmed uncertainties in dependence on Chl-a concentration. Low Chl-a concentrations tended to be overestimated and high Chl-a concentrations tended to be underestimated by the MODIS algorithm. The nearest coastal area up to about 10 km should be excluded in the investigations because of the strong deviations between measured and satellite derived Chl-a concentrations caused by misinterpretations in the atmospheric correction of MODIS. The linear regression analysis delivered high correlations between MODIS SST and measurements in the study area (N = 40, R<sup>2</sup> = 0.99, RMS = 0.056 K). The deviations were only up to 5%.

## 2.3. Hydrographic observations

At each station along the cross shelf transect vertical profiles of hydrographic parameters were recorded with a SeaBird SBE911 + CTD. It measured pressure, temperature, conductivity, oxygen concentration, chlorophyll-a fluorescence (683 nm), turbidity and photosynthetic active radiation (PAR). Additionally, the CTD-probe was equipped with a Rosette water sampler with 22 Free Flow bottles of 10 l volume. Each CTD cast started close to the sea surface with the pressure sensor usually at about 5 m depth. Data were collected down to 1500 m or 5 m above the bottom at shallower stations. The sampling rate of the CTD probe was 24 Hz. The CTD temperature sensors were validated during the cruise by comparison measurements with electronic reversal thermometers. Salinity samples were taken approximately once a day. Conductivity (then salinity) of the samples was determined by means

of a salinometer AUTOSAL Model 8400B (accuracy of 0.001). After postprocessing of CTD data the residual errors for temperature and salinity amount to 0.002 K and 0.003, respectively. The oxygen sensor was validated, using Winkler-titration of water samples (Grasshoff et al., 1983). The remaining uncertainty of the CTD derived oxygen concentrations is about ± 4 μM. Oxygen and nutrient concentrations are given in μM as abbreviation for μmol l<sup>-1</sup> (equal to mmol m<sup>-3</sup>). The calculation of SACW fraction below the surface mixed layer was performed according to Mohrholz et al. (2008), using the validated temperature and salinity data of the CTD. The uncertainty of the derived absolute SACW fraction values is well below 10%. Since temperature and salinity are conservative parameters below the mixed layer, a significant impact of biological activity on the SACW estimation is excluded.

In addition to the standard CTD on the first run of the transect a microstructure-turbulence profiler MSS 90-S (serial number 045) was deployed at each station, in order to obtain information about turbulent mixing and stability of the water column. The MSS is an instrument for simultaneous microstructure and precision measurements of physical parameters in marine waters. The profiler was equipped with two velocity microstructure shear sensors (for turbulence measurements), a microstructure temperature sensor, standard CTD sensors for precision measurements, an oxygen sensor, a turbidity sensor, and a vibration control sensor. All sensors are mounted at the measuring head of the profiler, the microstructure ones being placed about 150 mm in front of the CTD sensors to prevent disturbances. The sampling rate for all sensors was 1024 samples per second. At each station a set of 3 to 5 subsequent profiles was gathered. The profile to profile interval depends on water depth and ranges from 4 min in 60 m to 20 min in 500 m water depth respectively. The profiler was balanced with negative buoyancy, which gave it a sinking velocity of about 0.6 m s<sup>-1</sup>. It was operated via a dedicated winch from the stern of FS Merian. Disturbing effects caused by cable tension (vibrations) and the ship's movement were excluded by a slack in the cable. The dissipation rate of turbulent kinetic energy was calculated by fitting the shear spectrum to the theoretical Nasmyth spectrum in a variable wave number range from 2 to maximum 30 cycles per meter (cpm). The low wave number cutoff at 2 cpm is to eliminate contributions from low frequent tumbling motions of the profiler.

Moored instruments were used at two positions at the transect to observe the short term variability of currents, temperature and salinity in the water column within 40 m above the bottom. The mooring was deployed for the period from 24th August to 3rd September 2011 on the shelf (station 6) in 200 m water depth and from 7th to 17th September 2011 at the shelf break at 400 m water depth (station 11). The mooring was equipped with a bottom mounted current meter RDI Workhorse 600 kHz ADCP, and 4 SeaBird MicroCat thermosalinometers in depths of 2 m, 14 m, 26 m and 38 m above the bottom. Between the MicroCats additional temperature recorders (RBR TR1060, SeaMon) were mounted to enhance vertical resolution of the temperature measurements to 4 m. The ADCP was operated in Mode 12 to obtain data with low uncertainty level. Sampling interval was 2 s per profile. Each profile consists of 9 subsamples that are averaged without data screening. The uncertainty of single profile current velocities is about 0.02 m s<sup>-1</sup>. This is further reduced by temporal averaging during postprocessing. Sampling frequency of thermosalinometers was 15 s.

## 2.4. Nutrients

The inorganic nutrients ammonium, nitrite, nitrate, phosphate and silicate were measured in unfiltered samples using manual standard colorimetric methods (Rohde and Nehring, 1979; Grasshoff et al., 1983). The absorption was measured with a photometer Shimadzu UV1201V using 5 cm or 1 cm cuvette length depending on the intensity of the reaction color. The turbidity blank was measured for each sample and subtracted from the value. Standard sampling depths were 1, 10, 20,

30, 40, 60, 80, 100, 200, 400 and 600 m. The calibration was performed in regular intervals during the cruise and compared with experienced calibration factors. The following accuracy can be given: ammonium:  $\pm 0.05 \mu\text{M}$  (in the range under discussion), nitrite:  $\pm 0.02 \mu\text{M}$ , nitrate:  $\pm 0.10 \mu\text{M}$ , phosphate:  $\pm 0.02 \mu\text{M}$ , and silicate:  $\pm 0.10 \mu\text{M}$ .

### 2.5. Numerical simulations

A regional 3-dimensional coupled circulation and biogeochemical model was used to investigate circulation patterns and hydrochemical conditions on the Namibian shelf as a complementary approach during the time of the field campaign. The model domain covers the eastern boundary currents from the Cape region to the equatorial current system and extends into the open ocean to  $10^\circ\text{W}$ . The horizontal model resolution off Namibia is about 8 km. For details on the model grid, topography, open boundary conditions and subgrid scale mixing see Herzfeld et al. (2011). The ecosystem model is described in Schmidt

and Eggert (2012). The model is driven with realistic wind fields derived from scatterometer data (QuikSCAT, ASCAT). This data set has a spatial resolution of  $0.25^\circ$  and is a daily composite of 3 day periods. For more realistic results, daily cycles in wind speed and direction derived from 6 hourly NCEP winds are added (reanalysis data set from the National Centers for Environmental Prediction). The model was integrated over the model years 1999 to 2012. Five day averages for the simulated hydrographic fields, not only for currents but also for ecosystem variables like oxygen- and nutrient concentrations, are available for the last decade. For the period of the field campaign, 3 hourly model averages were stored. This allows also the study of the amplitude of inertial oscillations. Since the model is driven with realistic atmosphere data it can be validated by comparison with hydrographic quantities at cross-shore transects. The model results were compared with field data from several cruises. Sea surface temperature is also validated with remote sensing data (Muller, 2013). Fig. 3 shows the results of a “virtual cruise”, model data are extracted at the same time and position

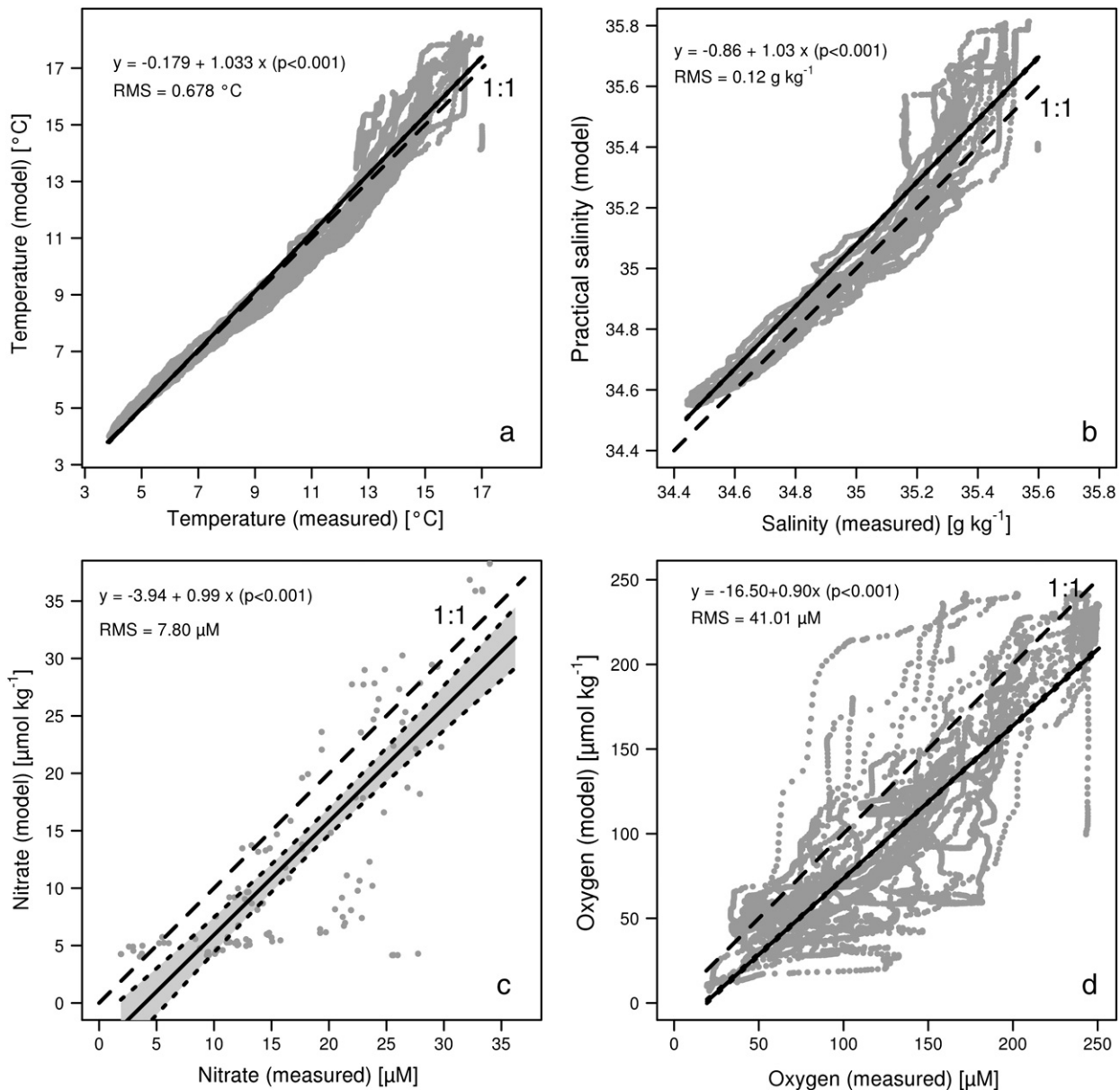


**Fig. 3.** Comparison of model results taken along a “virtual cruise” and field data (temperature, salinity, nitrate concentration, oxygen concentration) gathered on transect 4 during the SUCCESSION cruise. For temperature, salinity and oxygen concentration  $n = 12,385$  sample points are compared, for nitrate  $n = 130$ . The identity 1:1 line (dashed line) is drawn as a reference. The linear regression line (solid line) and its 95% confidence band are shown for each variable. The gray confidence band is, however, very narrow for temperature, salinity and oxygen as their sample sizes are very large. The formula of the linear relationship as well as the RMS are also given.

like in the field data. The scatter plots in Fig. 3 show the good correspondence between model results and field data, and also some model short-coming. As a tendency the model overestimates the SST in surface water (see also Muller, 2013). By comparison with radiation data from the ship weather station (not shown) this could be traced back to a bias in the NCEP short wave and long wave radiation. Accordingly, the gradients in the thermocline are too large and mixing requires too much potential energy. This also explains the positive salinity bias of the surface values and the negative bias in the subthermocline salinity. Also the enhanced mixing by breaking internal waves (see Results section) is not well represented in the model.

Biochemical variables like oxygen or nutrient concentration are influenced by more factors than the hydrographic variables temperature and salinity. Accordingly, the scattering of oxygen data is larger and the model results have a general negative oxygen bias. The fluctuations in the oxygen data reflect mostly the variability of the pole-ward under-current. Its position and strength are highly variable and the current forms subsurface filamental structures. Accordingly, the local gradients of the oxygen concentration are much larger than temperature or salinity gradients. Hence, a 1:1 correspondence between model and observations cannot be expected here. The negative oxygen bias corresponds to the strong local mineralization of organic matter. This is also the reason for the underestimation of nitrate data. Near the coast the oxygen concentration in bottom water is not sufficient for nitrification of ammonium to take place and nitrate concentration in the model is lower than that in the field data.

The simulation results provide information about how the SUCCESSION transect is embedded in the larger Benguela circulation pattern. The flow patterns allow us to determine to some extent the origin of water masses drifting through the area of field measurements. Simulation results were also used to carry out a “virtual cruise” along the investigated transect. Surface heat and oxygen fluxes of the numerical model were used to evaluate the calculation of the water mass pseudo-age. The high frequency numerical data also deliver an estimate for the hydrographic variability from inertial oscillations.

## 2.6. 'Pseudo-age' of surface water

One of the major concerns for the analysis of the interdisciplinary data sets is the differentiation between temporal succession in the ecosystem development and advection of the water masses, which is affected by mesoscale dynamics like filaments and eddies. This problem could be treated with floats that travel with a water parcel and allow a subsequent in situ sampling of the same aging water mass over a longer period. Also passive tracers like dye can be used to tag a water mass in

the field. However, the time scale of ecosystem succession in EBUS can be a few months. The effort to perform an interdisciplinary field program over this time is huge. Alternatively, water parcels with different age stages can be measured in a limited area (e.g. along a transect) in a short time. Then the particular measurements must be sorted along a time axis to perform the analysis of ecosystem succession. In this study the latter approach is used. For each station an independent age proxy 'pseudo-age' (PA) of the surface water mass was estimated, that is defined as the time after the first surface contact of upwelled water. However, as there is no conservative tracer to derive an age variable, temperature, oxygen and salinity were used instead. All variables are not conservative in the surface layer. Heat and oxygen flux through the surface, water evaporates and oxygen production and respiration by phytoplankton and zooplankton act as sources and sinks for oxygen and heat.

The aging of surface water splits into two subsequent periods governed by different processes, changing the water mass properties (Fig. 4). During the first period, directly after surfacing of the upwelled water, the temperature and oxygen concentration are considerably lower than those in the overlaying atmosphere. During this phase heat and oxygen fluxes are directed into the ocean and cause warming and ventilation of the surface layer. This phase corresponds to the linearly increasing branch in the temperature–oxygen (TO)-diagram (Fig. 4a). During the second aging period, the oxygen concentration in the surface water is largely balanced with the atmosphere and is close to the saturation level. In this phase, temperature is increasing through further heating and by lateral mixing with adjacent warmer oceanic waters. Since the oceanic water has also a higher salinity as the upwelled water, temperature and salinity increase with time and mixing stage. Concurrently, the density of the upwelled water is decreasing with time, due to warming. Fig. 4b depicts the nearly linear relation in the temperature–salinity (TS) space. The TO space and TS space were used for phases one and two, respectively, to construct the age proxy 'pseudo-age'. The boundary between both phases was recognized at an oxygen concentration of 182  $\mu\text{M}$ . The mean values of temperature, salinity and oxygen were calculated for the surface layer (0 to 25 m depths) at each station.

The PA is defined using the distance in the TO space between a reference point for freshly upwelled water ( $T_0 = 12.6^\circ\text{C}$ ,  $O_0 = 80.3 \mu\text{M}$ ) and the particular values at each sampling station. The anisotropy between temperature and oxygen concentration range in the TO plane is corrected by an empirical factor  $c_0 = 97.2$  that normalizes the range of temperature and oxygen concentration and weights both parameters equally. The distance is normalized with the maximum observed distance in the TO plane  $d_{\text{max}}$ . To convert the normalized distance into

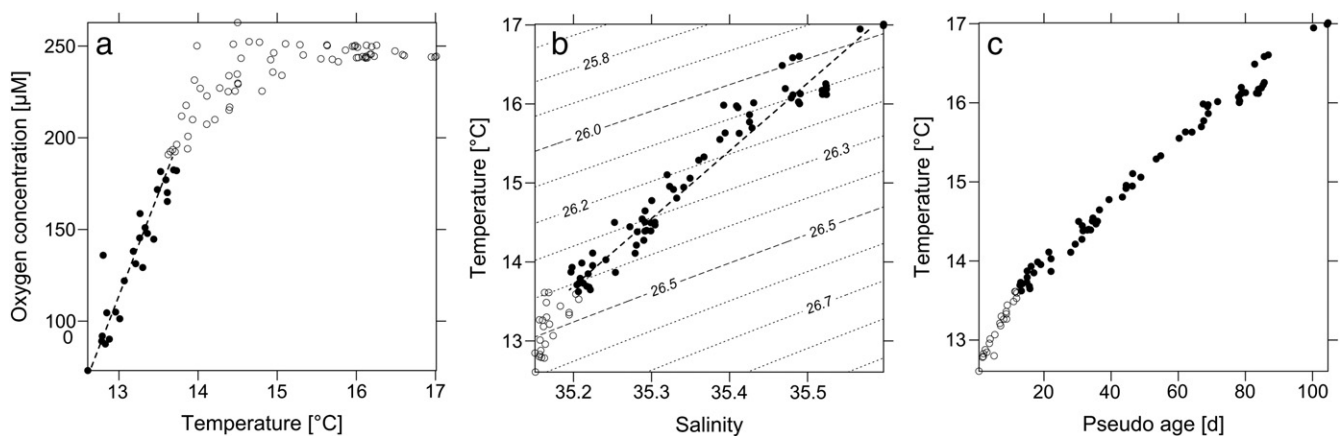


**Fig. 4.** Oxygen concentration vs. temperature (a) and temperature vs. salinity (b) in the upper layer (0–25 m) along the SUCCESSION transect based on CTD data. Black dots indicate the data points used for construction of the pseudo-age. Relation of temperature to pseudo-age of upwelled water along the transect (c). Open dots indicate PA data based on TO correlation, black dots indicate PA data based on TS correlation.

a time unit, the value is scaled by the mean offshore boundary  $x_1$  of the first aging phase (40 km) and the typical Ekman offshore drift velocity  $v_{E1}$  ( $0.035 \text{ m s}^{-1}$ ):

$$pa = \frac{\sqrt{(O-O_0)^2 + (c_o(T-T_0))^2} x_1}{d_{\max} v_{E1}} \quad (2)$$

For the second aging phase a similar approach was used based on distances in TS plane. The reference point was chosen from the water mass properties at the end of the first aging phase ( $T_1 = 13.6 \text{ }^\circ\text{C}$ ,  $S_1 = 35.18$ ). The anisotropy between temperature and salinity range in the TS space is corrected by a factor  $c_s = 0.12$ , normalizing the different ranges of temperature and salinity. For conversion of the normalized distance into a time unit, the value is scaled with the spatial extent of the second phase (western most station  $x_2 = 500 \text{ km}$  minus  $x_1$ ) and an average offshore drift velocity  $v_{E2}$  of  $0.06 \text{ m s}^{-1}$ . The 'pseudo-age' is corrected for the duration of the first aging phase ( $t_1$ ).

$$pa = \frac{\sqrt{(S-S_1)^2 + (c_s(T-T_1))^2} x_2 - x_1}{d_{\max} v_{E2}} + t_1 \quad (3)$$

The proxy 'pseudo-age' is highly correlated with both temperature and salinity (Fig. 4c). PA represents only a very raw estimate of the surface water age after upwelling. Due to the applied constant offshore drift, equal weighting of all parameters and the assumption of a linear relation between distance and time in parameter space PA has a high uncertainty, which changes in time and for each location. Even though PA is given in time units (days), PA has to be interpreted as an ordinal scale, i.e. the main purpose of PA is the ordering of the stations along a time vector to suppress the impact of advection by small and mesoscale processes on the study of ecosystem succession. The absolute value of PA should be used with caution. It depends on the particular parameter choice and will be biased to a certain extent. Regarding the absolute value of PA, especially the used offshore drift velocity is critical, but it will not alter the temporal order of the PA values.

### 3. Results

#### 3.1. Wind forcing

The wind forcing during the time of the cruise depicts some consecutive wind pulses of 2 to 10 days of duration, with intermediate phases of low wind speed. Typical wind speed was about  $10 \text{ m s}^{-1}$  during wind pulses and up to  $3 \text{ m s}^{-1}$  in between (Fig. 5). The shipboard wind observation time series reveals upwelling favorable wind conditions during four of the five performed transects. Whereas during T0 and T2 to T4 prevailing winds from east-south-east to southern direction were observed, the data measured during T1 shows winds from the northern direction. The wind speed is lowest in that phase and in the range of  $0.1 \text{ m s}^{-1}$  to  $4.7 \text{ m s}^{-1}$  (average:  $2 \text{ m s}^{-1}$ ). The measurements on T0 were performed during moderate wind speeds ranging from  $2.5 \text{ m s}^{-1}$  to  $7 \text{ m s}^{-1}$  (average:  $5 \text{ m s}^{-1}$ ). During T2 to T4 strongest wind speeds ranging from  $4.0 \text{ m s}^{-1}$  to  $14.3 \text{ m s}^{-1}$  (average:  $9.3 \text{ m s}^{-1}$ ) were observed.

Time series of wind speed and wind direction from the ship weather station and satellite derived DASCAT data compare well. The difference of the RMS is only  $0.4 \text{ m s}^{-1}$  for the wind speed and  $21^\circ$  for wind direction. Also spikes to be seen in the ship based data are resolved (Fig. 5). We conclude from the direct comparison of ship-based and scatterometer data that the quality of satellite data is sufficient for a discussion of the wind conditions during the cruise in the light of a wind climatology. The RMS difference is well below the maximum value of  $1.7 \text{ m s}^{-1}$  that Bentamy et al. (2008) found comparing DASCAT with buoy measurements. This confirms the high quality of scatterometer winds found by Kent et al. (1998).

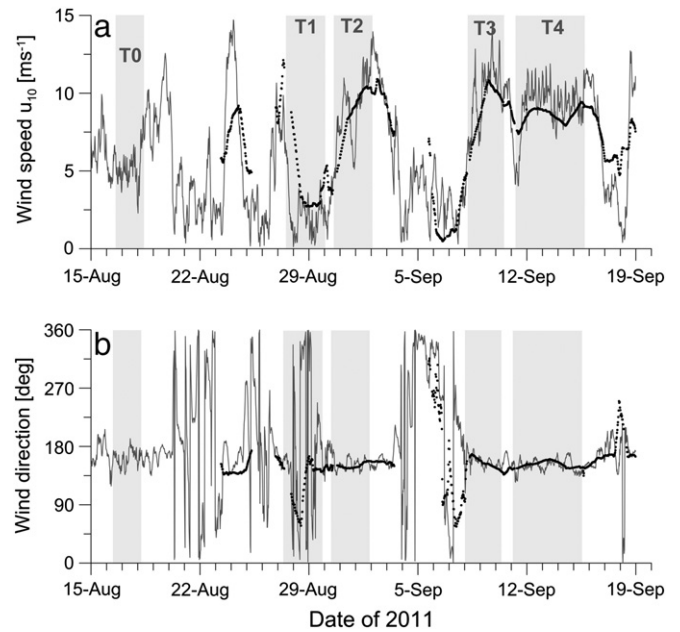
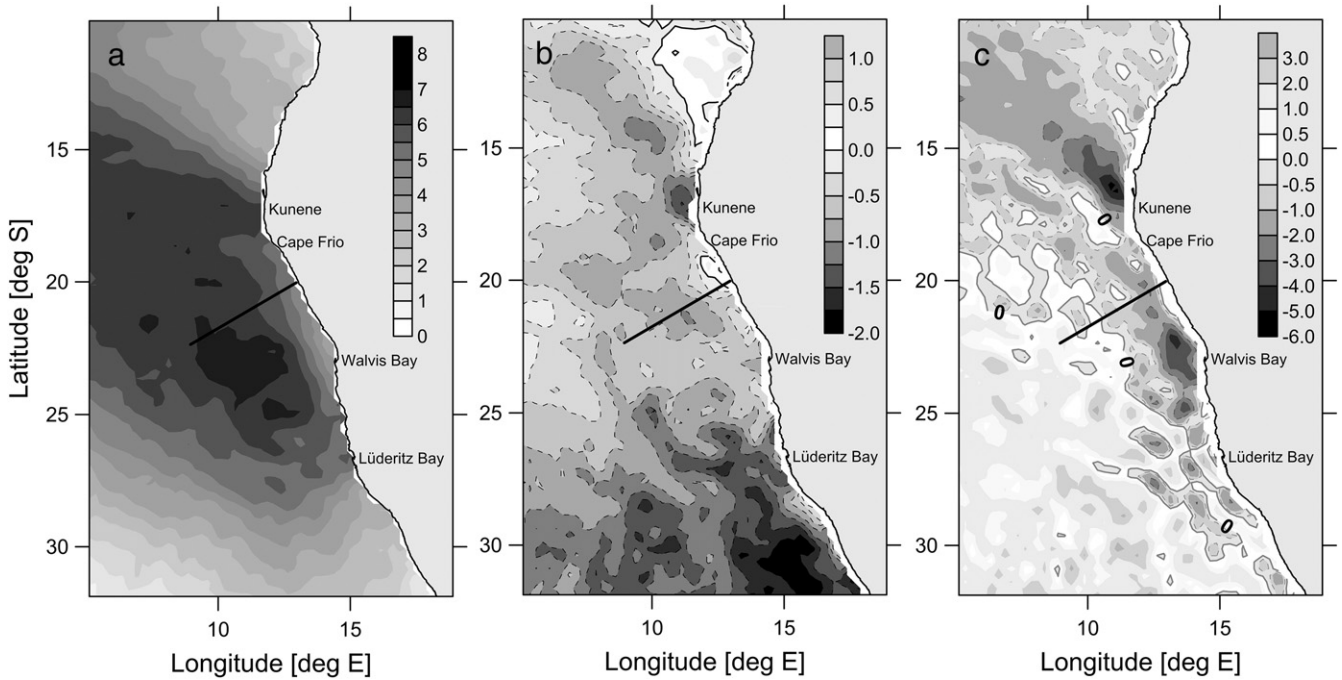


Fig. 5. Time series of wind speed (a) and meteorological wind direction (b) during the cruise, measured with the ship weather station onboard the R/V Maria S. Merian (lines). Scatterometer based data (ASCAT) at the ships position are overlaid as black dots. The five transects T0–T4 are marked by shaded background. Note that there is no satellite data at the ship position available when the position was too close to land, especially when the ship was in the harbor of Walvis Bay or during benthos sampling on the shelf. Daily DASCAT data were interpolated to ship positions for this comparison.

The spatial pattern of the average meridional wind speed during the cruise shows a cross shore gradient along the transect (Fig. 6a). Lower wind speed of values  $3$  to  $5 \text{ m s}^{-1}$  can be found at the inner stations within a narrow band between Cape Frio and  $25^\circ\text{S}$  along the coast. Between this locations only weak alongshore variance is observed. The offshore area is characterized by higher wind speeds in a broad band stretching from roughly  $28^\circ\text{S}$  to the north-west. Here the values range between  $5$  and  $7 \text{ m s}^{-1}$ .

To evaluate whether the upwelling season in 2011 was normal or exceptional with respect to wind forcing, the spatial DASCAT distribution was compared with the climatology SCOW. The two products, DASCAT and SCOW, originate from the two scatterometers ASCAT and QuikSCAT, respectively. Both show persistent differences during their period of overlap (11/2008–11/2009) (Bentamy et al., 2012). However, the temporal mean between collocated QuikSCAT and ASCAT wind speeds (QuikSCAT–ASCAT) is generally less than  $1 \text{ m s}^{-1}$ , but contains some planetary scale patterns. In the Benguela upwelling system the systematic offset between both platforms is close to  $1 \text{ m s}^{-1}$  (Bentamy et al., 2012). The zonal gradient of the meridional wind stress is the major contribution to the wind stress curl in the BUS assuming that the zonal wind stress is weak and zonal and meridional gradients of the wind stress are comparable. The absolute difference of meridional wind speed during the cruise from DASCAT (averaged over the period of the cruise) and SCOW climatological averages of August and September ranged between  $-2 \text{ m s}^{-1}$  and  $1 \text{ m s}^{-1}$  in the entire area off southwest Africa. Values are most negative in the southern Benguela upwelling system and are positive ( $1 \text{ m s}^{-1}$ ) in the north in the area of the Angola Dome, i.e. at  $12$ – $14^\circ\text{S}$  and  $10$ – $15^\circ\text{W}$  (Fig. 6b). In the proximity of the transect area, the difference is about  $0$  to  $-1 \text{ m s}^{-1}$  and of very small positive values in the very near shore area of the transect ( $0$  to  $+0.1 \text{ m s}^{-1}$ ). Considering the systematic offset between QuikSCAT and ASCAT wind speeds, the observed wind during the cruise in the area of the transect differs only very little from the climatological mean.



**Fig. 6.** Mean meridional wind speed [ $\text{m s}^{-1}$ ] during the period of the cruise (16.08.–19.09.2011) derived from DASCAT (a). Difference of the DASCAT mean meridional wind speed [ $\text{m s}^{-1}$ ] during the period of the cruise to the SCOW climatology (b). Wind stress curl derived from DASCAT data (c). The black line depicts the position of the SUCCESSION transect.

3.2. Seasonal variability of SST and SSS

The seasonal and interannual variability of the water mass distribution within the northern Benguela is also reflected by the SST variability as seen in remote sensing data. SST is often considered as a proxy for the “intense Benguela upwelling”, the IBU (Hagen et al., 2001). Additionally, the advection of warm saline water from the north as well as seasonal surface warming and cooling contributes to the variability of the SST (Shannon et al., 1986; Rouault et al., 2007). To include these processes in the discussion, the SST average within a stripe of 200 km width from the coast is considered (Fig. 7). The seasonal south-ward extension of tropical water ( $T > 20\text{ }^{\circ}\text{C}$ ) and its replacement by cooler water can be understood as annual poleward penetration of tropical water and its replacement by upwelled cooler water. Mohrholz et al. (2001) discuss the

dynamics of this process with an example of an event of south-ward propagation of tropical water and its subsequent detachment from the coast by the onset of upwelling to be seen as rapid cooling in remote sensing data. The position and the area enclosed by the  $20\text{ }^{\circ}\text{C}$  isotherm are a rough measure for the pole-ward spreading of tropical water. The  $15\text{ }^{\circ}\text{C}$  isotherm represents roughly the upwelled water. It turns out that the SUCCESSION cruise took place immediately after the maximum of the upwelling season. Comparing with four precedent years, 2011 is not an exceptional year. Considering the yearly average of the area enclosed by the  $13\text{ }^{\circ}\text{C}$  isotherm as a representation of the yearly IBU (Hagen et al., 2001) the value derived from MODIS monthly SST is very close to the total average from 2002 to 2012,  $14,000\text{ km}^2$ . Hence, in the light of the IBU upwelling intensity for the year 2011 is neither strong nor weak compared with the last decade.

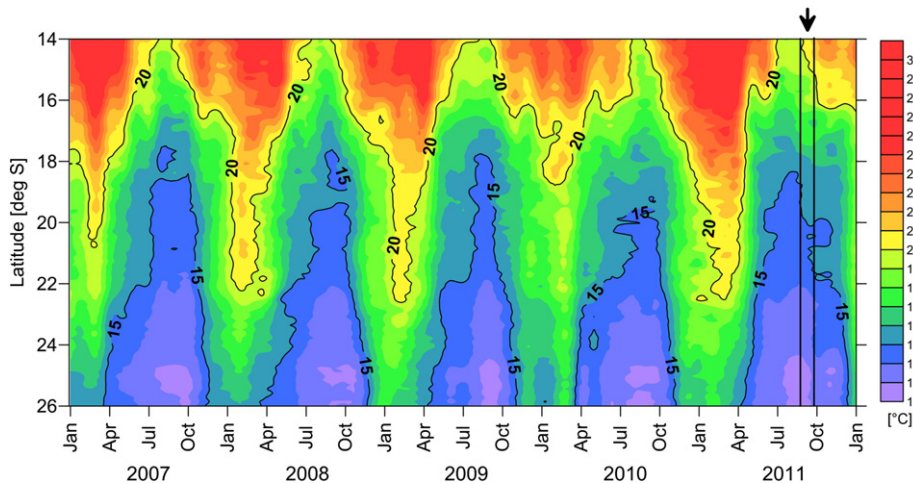


**Fig. 7.** MODIS SST within a stripe of about 200 km width from the coast, 2007–2011. Position of and area enclosed by the  $20\text{ }^{\circ}\text{C}$  isotherm represent the influence of tropical waters. The  $15\text{ }^{\circ}\text{C}$  isotherm encloses roughly the upwelled water. The arrow depicts the time of the SUCCESSION cruise.

### 3.3. Spatial SST and Chl-a evolution

Temporal and spatial development of SST and near surface Chl-a was investigated based on remote sensing data of the MODIS Aqua and Terra sensors. The short term variability of SST and near surface chlorophyll-a (Chl-a) distribution during the cruise is seen in high resolution satellite images in the vicinity of the sampling stations (Fig. 8). The observed structures depict the typical results of coastal upwelling, i.e. filaments with lower temperatures and higher Chl-a concentrations compared to the immediate vicinity. A nearly stable SST-filament (S1) was observed from 24th August to 3rd September 2011 which was dispersed around 14th September. Inside this filament the SST was up to 2.0 °C lower and the Chl-a concentration was up to 2.6 mg m<sup>-3</sup> higher than those in the surrounding waters. The inner stations of transects were located within this S1-filament, whereas the outer ones were influenced by up to 4.0 °C warmer, i.e. older water masses with up to 6.5 mg m<sup>-3</sup> lower Chl-a concentrations (S2). During the observation period the impact of various warmer water masses on different stations was increased (S3) or decreased (S4). Different persistent Chl-a-filaments (C1, C2) were observed. The stations in the middle of the cross shelf transect were influenced by the north-westward drifting C1-Chl-a filament. The C2-Chl-a-filament reached its maximum with up to 20.0 mg m<sup>-3</sup> around 2nd September 2011. Nearly all inner stations were situated within the Chl-a filaments on 24th August, but all stations were located outside on

14th September 2011. The small scale temporal and spatial variability, seen in Fig. 8, showed that the measurements along the cross shelf transect were influenced by different water masses. This fact supports the application of the pseudo-age approach.

### 3.4. Mean hydrographic and hydrochemical conditions

The observed thermohaline pattern is typical for a cross shelf transect through an active coastal upwelling cell in the northern Benguela. Only minor changes were observed between the five repeated transects. Within the surface layer temperature and salinity are decreasing from the offshore edge of the transect towards the coast from 17 to 13 °C and 35.56 down to 35.15 respectively. The strongest horizontal gradient was found within the first 100 km off the coast, where no pronounced thermocline was observed. The temperature at the coast of 12.5 to 13 °C implies that the upwelled water originates from 100 to 200 m depths. Seaward of the active coastal upwelling the surface layer of warmer and more saline water is approximately 70 to 90 m thick (Fig. 9). At about 300 km off the coast the surface layer is about 1 K cooler and less saline than the surrounding waters. This patch originates from the tip of the upwelling filament south of the transect (compare Fig. 8e) and illustrates the impact of mesoscale dynamics on the 2-dimensional picture of the transect measurements. In the central water layer below 100 m temperature and salinity decrease linearly

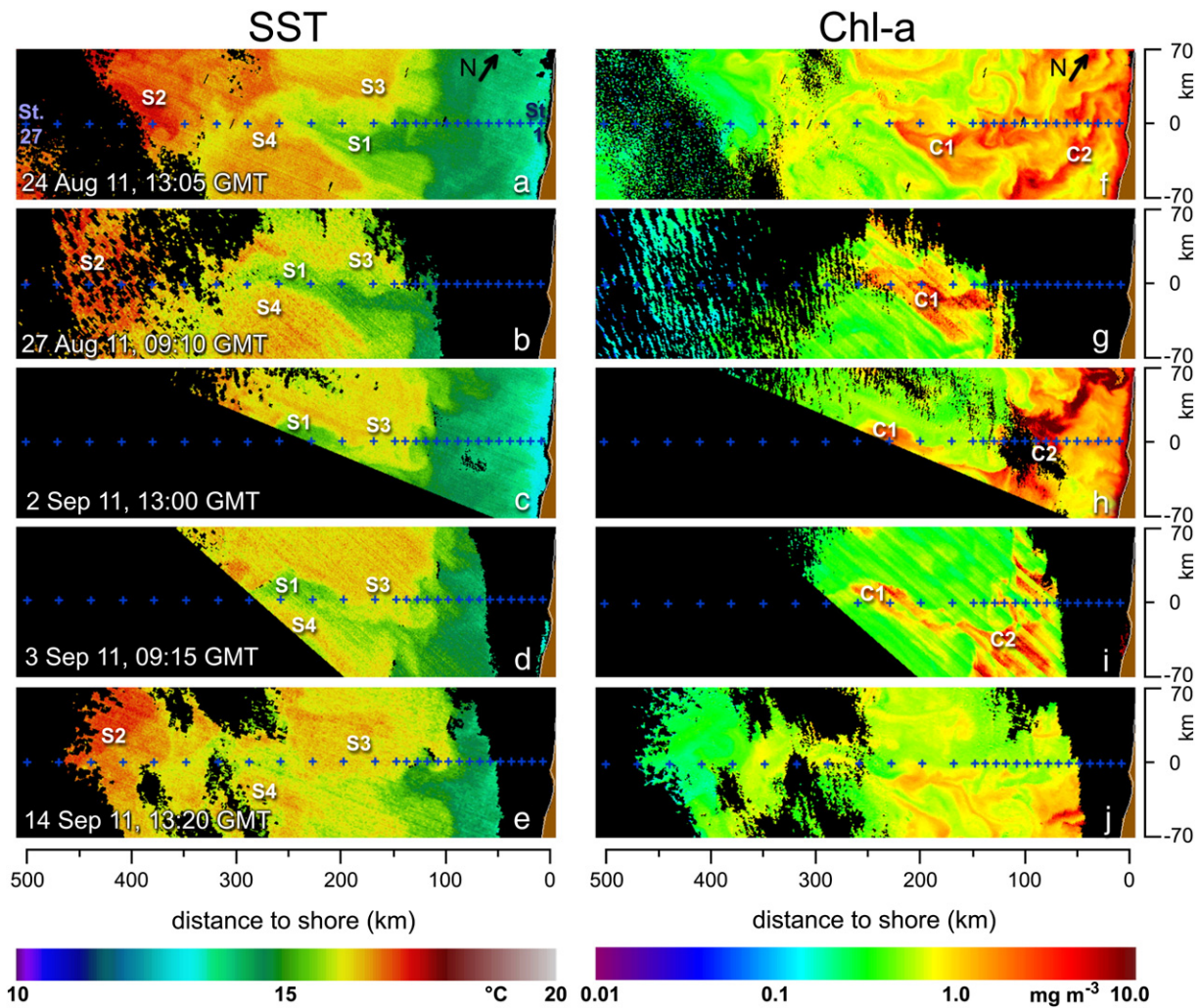


**Fig. 8.** The sea surface temperature (SST, a–e) and the chlorophyll-a concentration (Chl-a, f–j) of different MODIS scenes were shown up to about 500 km from the coast. The locations of stations 1 to 27 and different distinctive features were marked. The Namibian coast is located on the right hand side. Black areas characterized clouds or regions outside the satellite swath. All scenes were rotated to get horizontal alignment of transects.

from 14.5 °C and 35.32 at 100 m depth to 8.32 °C and 34.70 at 400 m depth respectively. In the central water layer vertical displacements of isotherms and isohalines with a scale of 20 to 40 m are observed, also detectable in the oxygen and nutrient distributions. Previous time series investigations have shown that these vertical excursions are caused most probably by internal waves, namely the internal tide (Mohrholz

and Heene, 2012). However, also the geostrophic adjustment of meso-scale dynamic patterns may cause some of these patterns.

The vertical distribution of dissolved oxygen is controlled by the ventilation of the mixed layer, advection of central water masses, biological processes in the water column and local oxygen demand of carbon rich sediments on the shelf (Fig. 9c). Outside the active upwelling at the

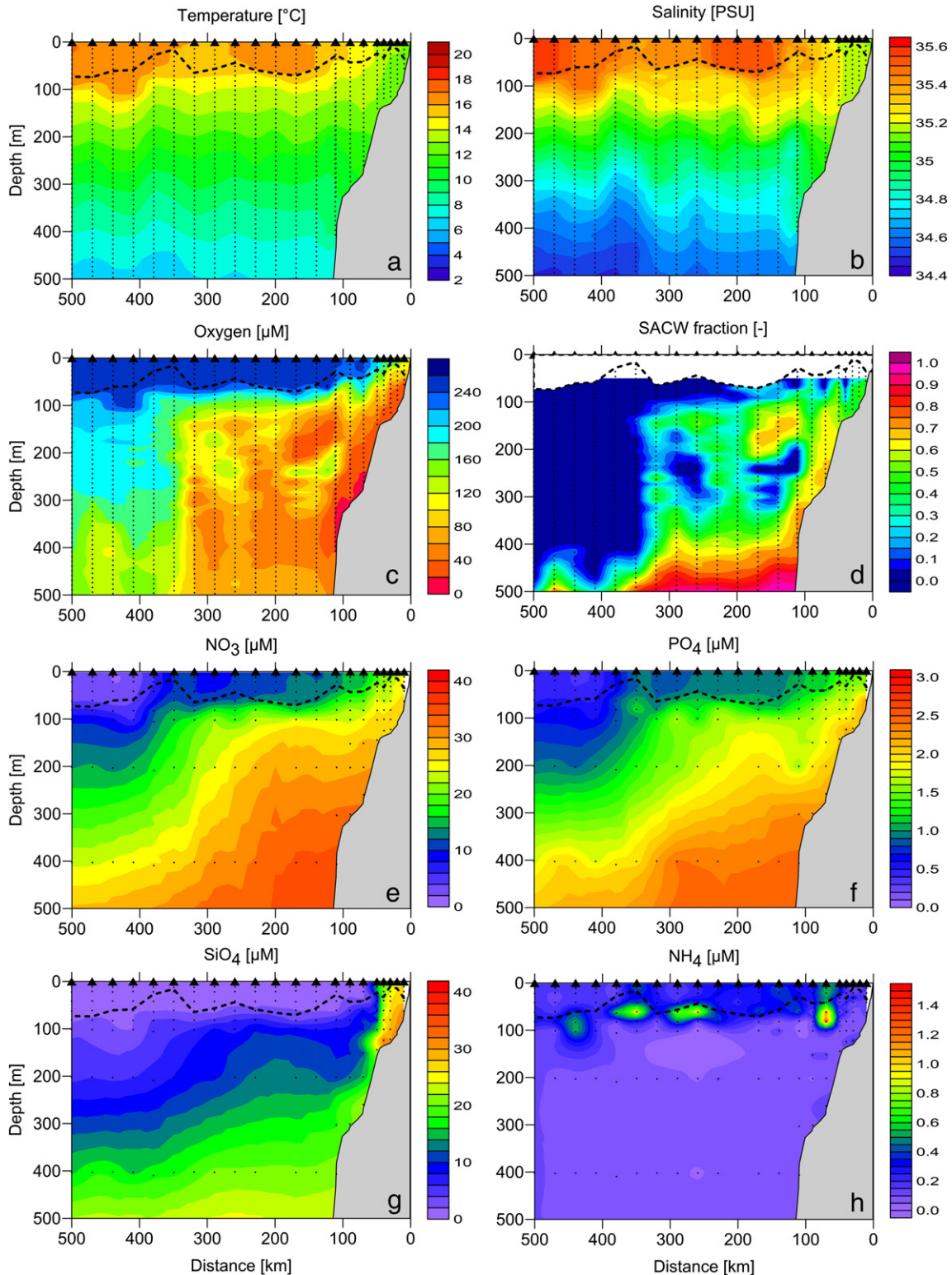


**Fig. 9.** Distribution of temperature, salinity, oxygen, SACW fraction and nutrients in the upper 500 m at the SUCCESSION transect. The dashed black line indicates the mixed layer depth. The data display the conditions during the fifth leg of the transect from 11th to 15th September 2011.

coast the surface layer is well ventilated down to 80 to 100 m by oxygen fluxes through the surface. Below 100 m a nearly vertical front between moderate ventilated and oxygen depleted water was observed at around 340 km distance from the coast (Fig. 9c). This boundary separates the SACW dominated region towards the coast from the pure ESACW, which was found in the open ocean (Fig. 9d). Between 100 and 400 m depths the SACW fraction varied considerably, pointing to an impact of mesoscale advection patterns. Maximum SACW fraction was found below 400 m depth and within the bottom layer on the shelf. SACW fraction and oxygen content of the central water layer are clearly negatively correlated in most areas. The higher the SACW fraction the lower is the oxygen concentration. However, especially on the shelf this correlation is disturbed by biological processes that act as local sources and sinks for oxygen.

Also the distribution of nitrate, phosphate and, to some extent, silicate is mainly determined by the central water distribution, with high concentrations in SACW and lower concentrations in ESACW (Fig. 9e–h). However, since the spatial sampling density is much smaller than that for the CTD data the distribution patterns of nutrients appear smoother. Generally, below the surface layer the nutrient concentrations increase with depth. At the coast the nutrients were lifted into the surface layer due to coastal upwelling dynamics. Here the maximum surface concentrations of nitrate ( $21.4 \mu\text{M}$ ), phosphate ( $1.66 \mu\text{M}$ ) and silicate ( $29.0 \mu\text{M}$ ) were found. However, the high concentrations of silicate over the inner shelf cannot be caused by upwelling alone, since the central water depicted lower silicate content. Possible mechanisms to maintain the high silicate concentrations at the coast are enrichment and terrigenous input of dust that is an important source for silicate and iron (e.g. Bopp et al., 2003). In the surface layer above 70 m the concentrations of nitrate and phosphate decrease with increasing distance to the coast. At the westernmost station 27 the surface concentrations of nitrate, phosphate and silicate amount to  $3.6 \mu\text{M}$ ,  $0.47 \mu\text{M}$  and  $1.4 \mu\text{M}$ , respectively. A detailed spatial and temporal description for the distribution

of dissolved inorganic nitrogen (DIN) and phosphate along the transects is given in Nausch and Nausch (2014—in this issue).

In contrast to nitrate and phosphate which were not exhausted even at the outermost station of the longest transect, silicate concentrations decreased in the surface layer quite rapidly. At the station nearest to the coast  $29.0 \pm 5.3 \mu\text{M}$  was measured. Already at station 5 only  $11.7 \pm 2.3 \mu\text{M}$  remained, decreasing further to  $3.7 \pm 3.3 \mu\text{M}$  at station 7 and reaching  $0.9 \pm 0.2 \mu\text{M}$  at station 18, the end of the short transects 1–3. Further out in the ocean (T4), silicate concentrations varied only slightly between 0.7 and  $1.7 \mu\text{M}$ . At concentrations below  $0.5 \mu\text{M}$  silicate became a limiting factor for diatom grow.

The ammonium distribution does not follow the picture described for nitrate and phosphate. The water layers below 100 m were characterized by very low ammonium values, close to the detection limit of the method of  $0.05 \mu\text{M}$  caused by nitrification processes. In the surface layer, ammonium concentrations are somewhat higher, ranging between  $0.09 \pm 0.04 \mu\text{M}$  (station 2) and  $0.35 \pm 0.26 \mu\text{M}$  (station 7). Interesting are spots of higher ammonium concentrations (Fig. 9) which occur occasionally and which may be the result of intensified mineralization processes or ammonia excreted by zooplankton. These patches seem to be confined with the edge of active upwelling at the inner shelf and with the edges of the upwelling filament that cross the transect at about 300 km off the coast.

During the first leg (T0) from 16th to 18th August microstructure measurements were carried out along the transect. Fig. 10 shows the dissipation rate for turbulent kinetic energy (TKE) and the Brunt-Väisälä frequency (BVF), as a measure for vertical stability of the water column. Maximum TKE dissipation of about  $10^{-6} \text{W kg}^{-1}$  is observed in the surface mixed layer and at some positions in the bottom boundary layer on the shelf. In the free water column the turbulence is generally weaker. Clear differences in the magnitude of TKE dissipation are seen between the shelf and the adjacent oceanic area, with a front at about 140 km off the coast. On the shelf the TKE dissipation is

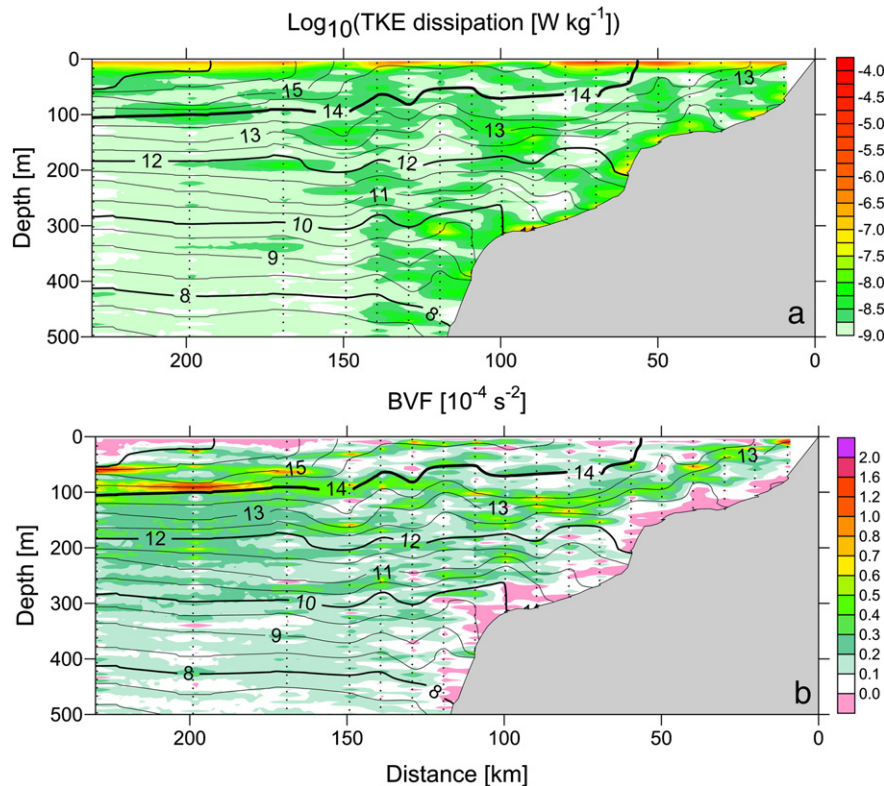


Fig. 10. TKE dissipation rate (a) and Brunt Väisälä frequency (b) overlaid with temperature (black isolines) along the SUCCESSION transect. High dissipation rates in the surface layer and above the bottom coincide with weak or instable stratification (low BVF).

more intermittent, but significantly higher. This coincides with enhanced vertical displacements of isotherms on the shelf, indicating the presence of internal waves. At the shelf break (350–400 m depths) the vertical isotherms also point to enhanced mixing. The enhanced dissipation on the shelf is caused by the interaction of internal tide with the topography (Mohrholz and Heene, 2012). At the shelf edge the bottom slope is at the critical value for breaking of internal waves with tidal period of M2. Breaking events of the internal tide generate nonlinear internal wave packages that travel onto the shelf (Nash et al., 2004). Their scattering and decay enhance the TKE level and turbulent mixing on the shelf. The BVF has maximum values at the bottom of the surface layer along the strongest vertical temperature gradient. The thermocline temperature is about 13 °C on the shelf and increases to 14.5 °C westward of the shelf break. Below the thermocline the water is stably stratified, with exception of the bottom layer on the shelf and the shelf break. Here the BVF is close to zero in a bottom layer of 30 to 50 m thickness.

The temporal variability of bottom layer conditions on the shelf was observed using moored instruments subsequently deployed midshelf (station 6, 200 m depth) and at the shelf edge (station 11, 400 m depth). On the shelf at 200 m depth bottom temperatures ranged from 11.6 to 12.4 °C during the mooring deployment from 24th August to 4th September. The temperature time series measured at 2 m and 38 m above the sea bed are shown in Fig. 11a. Strong temporal fluctuations were observed in both layers. Although the time series are too short for a spectral analysis, the visual inspection reveals fluctuations with periods from hours to about 2 days. The temperature fluctuations of both layers are correlated. At the shelf edge the temperature time series obtained in the bottom layer were very similar to those of the on shelf conditions. Here the near bottom temperature ranged from 8.7 to 9.8 °C (Fig. 11b). The short term temperature fluctuations 2 m above sea bed were slightly higher than those on the shelf. At both positions an upward looking ADCP provided current profiles of the near bottom layer (2–40 m above seabed). The spectral analysis of current meter data reveals significant signals in the M2 tidal and inertial frequency band, with periods of 12.4 h and 35 h respectively (not shown). On the shelf the tidal currents had a magnitude between 0.03 and 0.10 m s<sup>-1</sup>. Current velocities in the

inertial frequency band ranged between 0.02 and 0.06 m s<sup>-1</sup>. Using a low pass filter with a cutoff period of 48 h the mean current velocity was estimated (Fig. 11c). It was poleward directed with average meridional velocity of about -0.06 m s<sup>-1</sup>. The cross shelf current velocity was close to zero. At the shelf edge the current field depicted a comparable behavior. The mean flow was also poleward directed, but with slightly slower velocities of about -0.04 m s<sup>-1</sup> (Fig. 11d).

### 3.5. Hydrographic and current fields – the model view

The numerical simulations with the 3D model provide comprehensive information on time- and spatial scales and reach a high resolution coverage that cannot be obtained from in situ observations. The modeled distribution of temperature and salinity as well as of currents was stable during the period of the cruise. Fig. 12 depicts a typical pattern observed in the simulation results. At the coast there is a band of cold (and less saline, data not shown) water. Its lower temperature indicates that it welled up recently. Within this thin band of cold water stretching along the coast, there exists a so called coastal jet. Its core with maximum velocity is found at the sea surface near the coast, but it penetrates down to 80 m depth. The average northward surface flow speed amounts to 0.12 m s<sup>-1</sup>. Occasionally it accelerates to 0.25 m s<sup>-1</sup>. During the time of the cruise the average velocity variance amounts 0.07 m s<sup>-1</sup> within the core of the jet.

Offshore, the surface currents are mainly governed by a north-westward Ekman transport, which determines the mean flow direction. From its permanent presence arises the idea of a trophic succession within water bodies drifting off-shore. However, the surface flux is not uniform. From baroclinic instability emerge areas with enhanced or reduced surface flow carrying water with different densities and corresponding to different mixing depths. As shown by Muller et al. (2013), these current patterns become geostrophically balanced and persistent so that filaments may develop. The model results (Fig. 12a) reveal the currents related to the mesoscale filament pattern seen in the observed SST data (see Fig. 8). The filaments continue below the mixed layer depth that varies typically from 20 m to 60 m but may exceed 100 m intermittently and far off-shore (Fig. 12b). Here the flow is less directed and there are also eddies and jet-like currents directed in-shore.

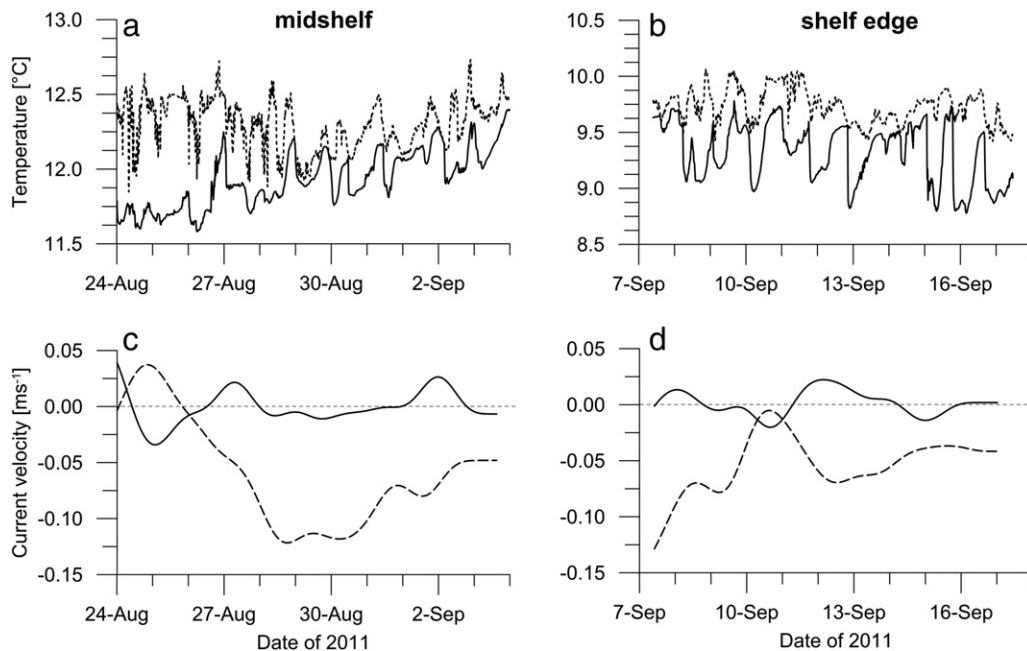


**Fig. 11.** Time series of temperature (a, b) and current velocity (c, d) in the near bottom layer on the shelf (left, 200 m depth) and on the shelf edge (right, 400 m depth). The current velocities are low pass filtered with a cutoff time of 48 h and vertical averaged over the 4 to 40 m above sea bed. Plots a and b: temperature 2 m above sea bed solid line, temperature 38 m above sea bed dashed line. Plots c and d: eastward current velocity solid line, northward current velocity dashed line.

Hence, the model results support the idea that the cruise is carried out in water masses drifting off-shore starting from the coast. Water masses near the coast are considered as “young”, they are influenced by coastal upwelling, are cold and oxygen depleted, and carry nutrients, and new production may start. With time the surface water grows older and takes up heat and oxygen from the atmosphere and ambient waters, nutrients become consumed and a plankton community develops. Within a uniform off-shore flow “age” would correspond to “drift time” and hence to “distance from the coast”. However, the enhanced surface flow within the filaments introduced some disorder and there are obviously intrusions of younger water masses within older water bodies (see Fig. 12a). This finding can be verified from the SST images (see Fig. 8) and supports the idea of introducing a ‘pseudo-age’ of water masses to relate the trophic succession to hydrodynamic processes. However, below the thermocline the simulated flow pattern indicates a meandering poleward undercurrent generating eddies instead of an evenly directed flow, which limits this idea to the surface layer, where the directed Ekman flow overwhelms (Fig. 12b).

At time scales shorter than the inertial period, the flow patterns become much more variable. Intermittently strong inertial oscillation can be observed within the mixed layer (not shown). Below the mixed layer depth weak periodic flow indicates radiation of inertial waves. The maximum velocity at the surface is about  $0.25 \text{ m s}^{-1}$ . The corresponding radius of the inertial oscillations is about 3 km. This is considerably smaller than the baroclinic Rossby radius (Houry et al., 1987). Thus, only minor uncertainties should be caused by the small scale processes when sampling along the transect is not in phase with the inertial oscillations.

### 3.6. Temporal variability of hydrographic conditions

In order to investigate the temporal variability of surface layer conditions the in situ data were compared to the model results using a Hovmöller plot (Fig. 13). The absolute values of in situ and model temperatures and salinity differ considerably. Model temperature and salinity exceed the observations by about 2 K and 0.3 respectively. However, the temporal behavior of temperature and salinity patterns was comparable. At the coast both data sets show the cold and less saline water belt of upwelled water with a similar width and offshore temperature and salinity gradients. The temporal variability of the upwelling belt is rather low in both model data and observations. The model data show small short term fluctuations in inertial period, which cannot be resolved by the in situ data. However, these fluctuations have no significant impact on the large scale patterns. A remarkable feature is the offshore advecting patch of cooler water, also reproduced by the model. This structure is associated with an offshore moving filament (compare Fig. 8). The position of the patch in the model was shifted slightly offshore by about 50 km. The estimated offshore velocity of this patch is about  $0.06 \text{ m s}^{-1}$ . For comparison the mean Ekman velocity

in the mixed layer ( $H_{\text{mix}}$ ) during the cruise from wind data is calculated using:

$$u_{\text{Ekman}} = \frac{\tau^{(y)}}{\rho f H_{\text{mix}}} \quad (4)$$

The mean observed meridional wind speed in the vicinity of the coast was in the order of  $5 \text{ m s}^{-1}$  (see Fig. 6a). This value corresponds to a mean wind stress of  $9 \cdot 10^{-2} \text{ N m}^{-2}$ . Assuming a mixed layer depth of  $H_{\text{mix}} = 20 \text{ m}$  the Ekman velocity can be estimated to be in the order of  $0.07 \text{ m s}^{-1}$ . This value compares well to the drift velocity of the observed filament.

The oxygen concentration in model data and observations shows the highest difference at the coast. In the model the oxygen concentration in newly upwelled water is about 60 to 70  $\mu\text{M}$  higher than that in the observations (Fig. 13). Outside the coastal upwelling belt the differences are low and mainly controlled by temperature variability and by the distribution of chlorophyll-a that acts as oxygen source. In the deeper layers the model underestimates the oxygen concentration (see Fig. 3d). Too high oxygen concentration in the upwelled water implies too weak vertical exchange with the water body below the mixed layer. Several factors may contribute, but details are not clarified yet. Unresolved topography, too coarse wind fields, but especially the roughly parameterized mixing driven by breaking internal waves, is under investigation. Finally, the overestimation of oxygen concentration near the coast could be caused also by the oxygen release from the rapidly growing model plankton in the coastal belt, which is not seen in the in situ Chl-a fluorescence data. The distribution of phytoplankton, measured as Chl-a fluorescence in the field and estimated as chlorophyll-a concentration in the model, depicts large differences between model output and observations. This is not surprising since in situ fluorescence measurements are affected by small scale patchiness of phytoplankton, light conditions, species composition and many other factors that were not implemented in the model. A calibration of in situ Chl-a fluorescence with chlorophyll-a measurements from bottle data was not possible, due to the low number of samples. The modeled chlorophyll-a concentrations are based on the nitrogen content of phytoplankton, with the assumption of a fixed Redfield ratio. In the model, the maximum Chl-a concentration is found near the coast with only small temporal fluctuations. A secondary maximum is confined to the offshore patch of upwelling water. In situ data show enhanced Chl-a fluorescence 50 to 150 km off the coast and also in the patch of offshore moving upwelling water.

## 4. Discussion

The data presented in this study describe the hydrographic and hydrochemical conditions during a “normal” upwelling situation in

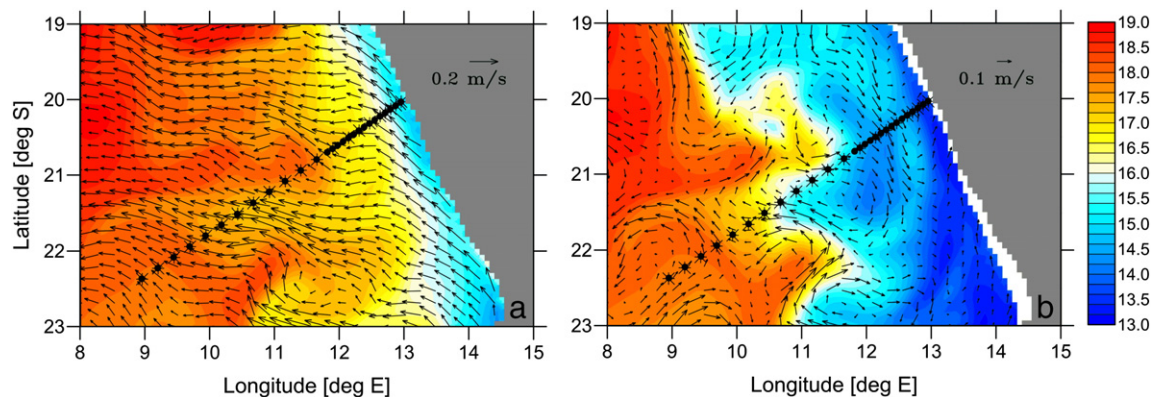
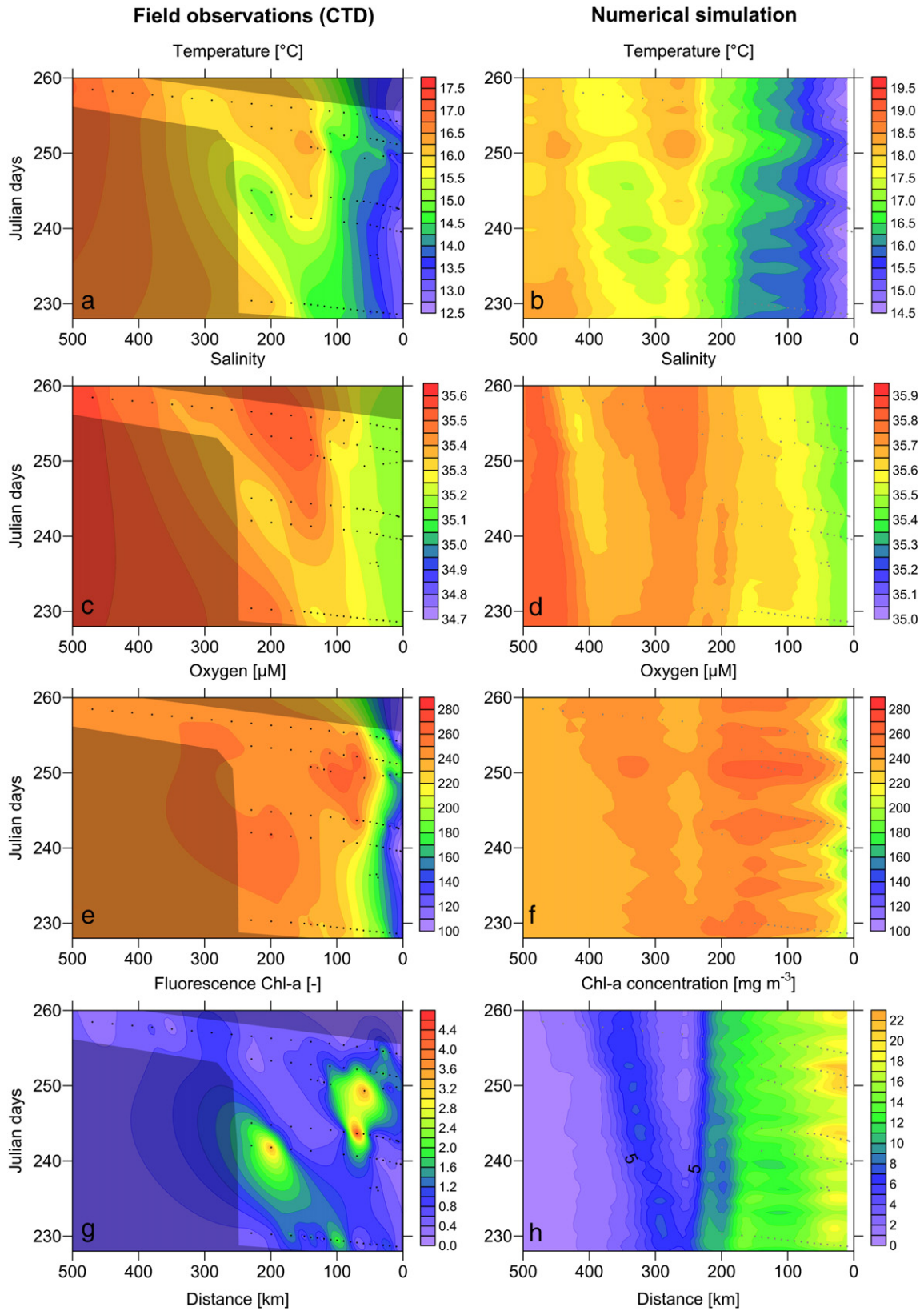


Fig. 12. Five day averages of potential temperature and current field from the numerical simulation for the beginning of September 2011. Vertical average over the upper 20 m (a) and conditions at 75 m depth (b).

austral winter in the northern Benguela upwelling system. In August and September 2011 the average meridional wind speed was very close to the climatological value, derived from scatterometer winds.

Also the yearly averaged index for “intense Benguela upwelling” (IBU, Hagen et al., 2001) derived from monthly MODIS data supports this view. The IBU was very close to the average over the last decade.



**Fig. 13.** Hovmöller plot of temperature, salinity, oxygen and chlorophyll-a along the transect, vertically averaged from the surface to 20 m depth. Left panels based on CTD data. Right panels depict the output of the numerical simulation. Black dots indicate the positions of CTD casts. The color scales consider the model bias of 2 K and 0.3 g kg<sup>-1</sup> for temperature and salinity, respectively.

This means that the amount of upwelled water drifting through the SUCCESSION transect represents typical conditions. This also implies that filaments seen in the hydrographic, remote sensing and model data are usual phenomena and need consideration in the discussion of the field data and model results.

#### 4.1. Curl and divergence driven upwelling

Coastal upwelling and curl driven upwelling have different effects on the ecosystem structure and productivity (Rykaczewski and Checkley, 2008). Thus, it is important to distinguish between both mechanisms and to determine its relative contribution to the vertical velocity. In order to estimate coastal upwelling we use an idealized analytical model by Fennel and Lass (1989) and neglect alongshore and cross-shore variations of the wind stress. The strength of coastal upwelling can be estimated from an idealized two dimensional analytical model (Fennel, 1999). Alongshore and cross shore variations of the wind stress are hereby neglected. In this case, the response of the coastal ocean is two dimensional (independent of the alongshore coordinate) (Philander and Yoon, 1982). Moreover we assume that the barotropic mode of the vertical velocity is small since it is diminished by the very fast barotropic Kelvin wave anyway. The wind stress that drives the analytical model was roughly estimated from the time averaged wind stress near the coast. The following parameters went into the analytical model: The first mode Rossby radius has been assumed to be  $R_1 = 15$  km, the mean water depth on the shelf is  $H = 200$  m, the mean BVF is  $N = 0.01 \text{ s}^{-1}$ , and the mixed layer depth is  $H_{\text{mix}} = 20$  m along the transect. However, the integrated vertical transport depends primarily on the used wind forcing. The parameters  $R_1$ ,  $H$ , BVF and  $H_{\text{mix}}$  control mainly the spatial structure of the upwelling dynamics, as the width of the upwelling belt at the coast and the vertical structure of the current patterns.

Curl driven upwelling was estimated from Eq. (1) using the mean wind stress curl data presented in Fig. 6c. Both processes, curl driven upwelling and coastal upwelling, are included in the numerical circulation model. Hence, the simulation fields can be used to verify our analytical approach. Moreover the simulation results allow a more general estimate of the upwelling strength since they also include the influence of coastal shelf waves, Rossby waves and mesoscale variability on the upwelling strength.

The mean vertical velocity component estimated from both upwelling mechanisms and the results from the numerical circulation model at the mixed layer depth ( $H_{\text{mix}} = 20$  m) are presented along the transect in Fig. 14a. Coastal upwelling is basically confined to the coast within a 50 km wide band. The largest vertical velocity related to coastal upwelling is observed near the coast where values of  $3 \cdot 10^{-5} \text{ m s}^{-1}$  ( $2.6 \text{ m d}^{-1}$ ) are reached. Further offshore coastal upwelling decreases rapidly. Wind stress curl driven upwelling is very small in the vicinity of the coast but positive up to about 300 km from the shore. The results indicate that most of the curl driven upwelling takes place within a zone between 50 and 250 km offshore. It reaches a maximum of  $4 \cdot 10^{-6} \text{ m s}^{-1}$  ( $0.35 \text{ m d}^{-1}$ ) at about 90 km. This upwelling maximum corresponds to the wind stress curl maximum along the transect clearly observed in Fig. 6c. Further offshore than 400 km the curl driven vertical velocity becomes negative due to the switch in sign of the wind stress curl (Fig. 6c). The vertical velocity derived from the numerical circulation model is in the order of the analytical approaches. The rapid increase of coastal upwelling towards the coast corroborates the analytical model results regarding strength and spatial shape of the vertical velocity. Further offshore the numerical model results exhibit a high spatial variability that may be attributed to physical processes that are not captured by the analytical approach such as eddies, filaments or Rossby waves.

The estimated cumulated vertical transport from both upwelling mechanisms as well as from the numerical model is presented in

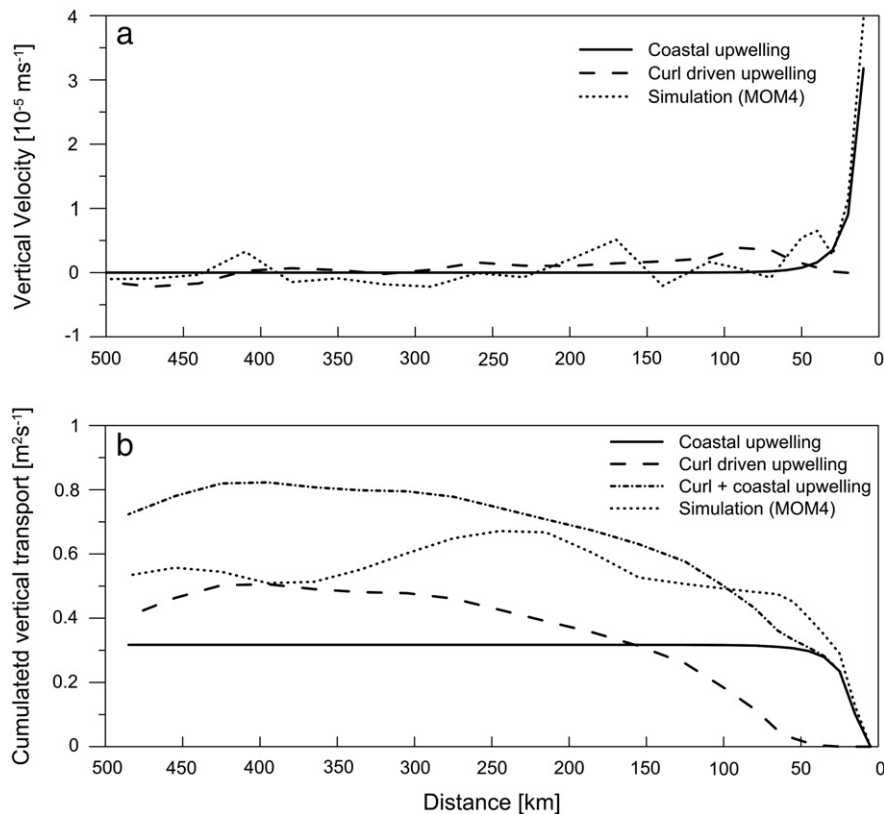


Fig. 14. Different approximations for upwelling strength in (terms of vertical velocity), solid line: the coastal upwelling from the analytical theory, dashed line: upwelling driven by the wind stress curl, dotted line: results from the numerical simulations. Upper panel (a) depicts the upwelling velocity at  $z = H_{\text{mix}}$ , lower panel (b) shows offshore cumulated vertical transport.

Fig. 14b. The cumulated vertical transport depicts the amount of water transported by the different upwelling processes into the euphotic layer along the transect. Cumulated coastal upwelling converges very fast to a constant value of about  $0.3 \text{ m}^2 \text{ s}^{-1}$ . It is exceeded by the curl driven cumulated vertical transport offshore of 150 km distance to the coast. Upwelling vanished at about 330 km offshore distance. The combination of cumulated coastal and curl driven upwelling matches roughly with the results from the numerical model along the transect. Nevertheless, the maximum of cumulated transport combined from curl and coastal driven upwelling can be found 150 km further offshore than the numerical model results explain. Cumulated along the entire transect the curl driven upwelling exceeded the coastal upwelling by about 50%. Thus, upwelling indices based only on the extent of the cold water belt near the coast or onshore–offshore temperature gradients may be considerably biased, since only the coastal upwelling is recognized.

#### 4.2. Water mass distribution and advection

The patterns of hydrographic and hydrochemical parameters in the northern Benguela are mainly determined by the special shape of wind forcing and the distribution of central water masses. The wind driven upwelling lifts nutrients from the central water into the euphotic layer. This happens with high vertical velocities near the coast and by slow wind stress curl driven entrainment at the bottom of the surface mixed layer in the belt of negative wind stress curl. However, also the distribution of central water was influenced by the wind field. The meridional current in the eastern subtropical gyre of the South-Atlantic can be described by the Sverdrup balance (Lass and Mohrholz, 2008), where the meridional transport on the  $\beta$ -plane is proportional to the wind stress curl. In the Sverdrup balance negative wind stress curl causes a poleward transport and vice versa. Since the two source water masses SACW and ESACW enter the northern Benguela from opposite sites, their general distribution is controlled by the meridional currents. The poleward movement of SACW is confined to the belt of negative wind stress curl close to the coast. Northward ESACW advection is connected to the Benguela current, the eastern branch of the subtropical gyre. The location of boundary between SACW and ESACW on the SUCCESSION transect was found at the position of maximum wind speed i.e. at the boundary between negative and positive wind stress curl regions

(compare Figs. 9d and 6c). This confirms with the prospects derived from the Sverdrup balance.

Via the water mass distribution the wind forcing has also an impact on the nutrient supply to the surface layer. In areas where SACW dominates, the nutrient supply by entrainment at the bottom of the mixed layer is higher than that in the case of ESACW dominated central water. This is caused by both the lower nutrient concentrations of ESACW and the lower entrainment, due to changes in wind stress curl. The nitrate and phosphate concentrations in surface water drop down at the underlying SACW/ESACW boundary (Fig. 9d–f). At this position the offshore gradient in nutrient concentrations is significantly enhanced.

A major issue in this study is the applicability of the 2-dimensional conceptual model suggesting succession processes in the upwelling area. The numerical simulation shows how the 2D-hydrographic data were embedded in the South-Atlantic circulation. The time average of surface currents reveals that the current direction is almost perpendicularly to the sampled transect. Because of the small temporal variability of the wind field this flow pattern is observed permanently during the cruise. This implies that water drifting through the different parts of the transect originates from different sources. Hence, the comparison of data from different stations requires the additional assumption that the source areas of the upwelled water masses behave similar. The flow lines shown in Fig. 15 suggest that most surface water stems from a long upwelling band stretching along the Namibian coast. Here the hydrographic conditions are similar. Also the constant excess phosphate (Nausch and Nausch, 2014–in this issue) found at all stations supports the hypothesis of similar source water masses. This is also seen in the model results, with exception of the coastal stations and the three outmost stations (not shown).

Fig. 15 shows a dichotomy of the southern ocean, especially in the area of investigation. It is influenced by water masses of either northern or southern origin. The figure shows results of a numerical tracer release experiment, carried out in the equatorial undercurrent, in the SACW in the Angola Dome area and in the Cape region. In the source regions the tracers are “released” permanently so that its concentration is kept to unity. Hence, the total amount of released tracers depends on their residence time in the source area. Fig. 15 shows the surface concentration at the time of the field campaign, which has developed after 12 years of model integration. For comparability, the surface concentration is

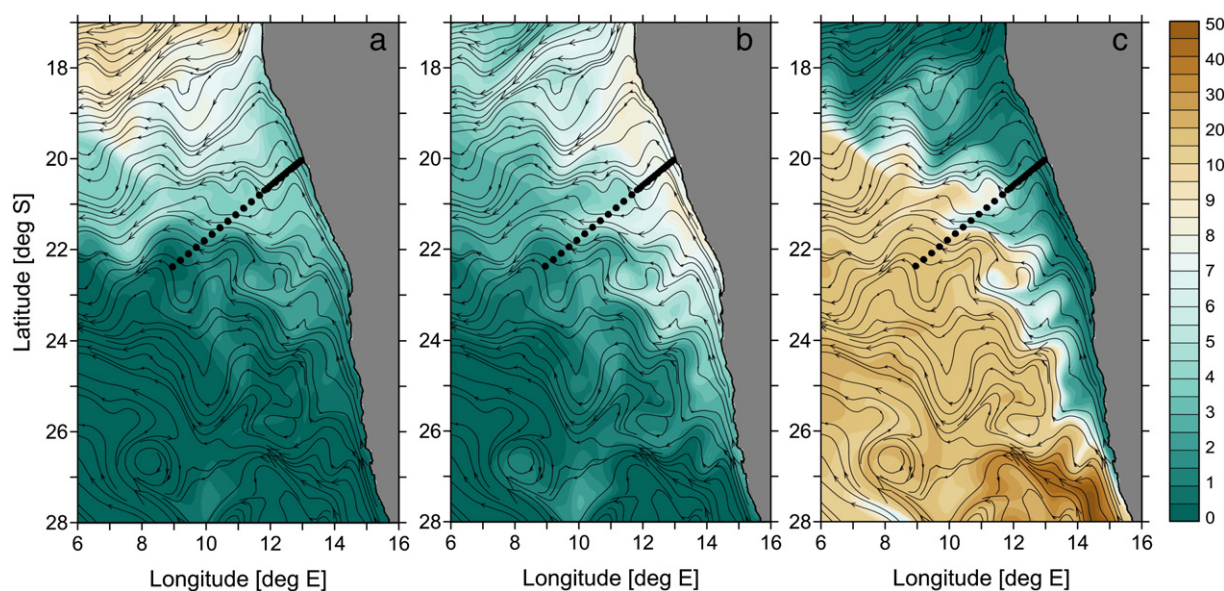


Fig. 15. Distribution of passive conservative tracers and flow lines averaged over the period of the cruise from 23rd August until 20th September 2011 (0–20 m depths). The points mark the stations along the transect. The figure shows the differences in tracer distribution between the tracer released in the equatorial undercurrent (a), the Angola Gyre (b) and another one released in the Cape region (c). The tracer concentration is given as the dimensionless ratio between the local tracer concentration and the tracer concentration averaged over the upper 1000m of the total model domain. The flow lines are derived from the averaged currents as a simple guess for the drift path a water parcel would have for constant currents.

weighted with the average tracer concentration of the full model area in the upper 1000 m. This way, the tracers may be considered as fingerprints left behind by the source region of the tracers. The coastal waters carry the fingerprints of the Angola Dome area, the passive tracer originating from there is brought to the surface in the long coastal upwelling band. Its signature vanishes at about 25°S. Almost all water except the out-most stations is influenced by this water mass. Notably, the filament influencing the central stations with colder and less saline waters carries its signature. Water with enhanced fingerprint of the equatorial undercurrent is also found at most stations except the out-most stations and the station in the coastal upwelling area. It is spreading pole-ward in the surface flow and not with the undercurrent. It cannot penetrate to the south as far as the Angola Dome water does. Waters with a fingerprint from the surface waters of the Cape region influence the out-most stations, but are also found more in-shore within eddy like flow pattern. The Cape fingerprint is not left behind in all ESACW, the surface distribution of this tracer marks only a part of the ESACW.

Finally, in the model results the outmost stations are not influenced by water from the pole-ward current system but show a great influence of ESACW. This water mass has slightly enhanced salinity. Nevertheless, the flow lines suggest that the surface water at the outmost stations has also had contact with the shelf. A direct correspondence between model and measurements cannot be expected for a highly non-linear eddy flow pattern, but a similar signal of enhanced salinity is also seen in the hydrographic data.

Optical in situ and satellite measurements verified the special character of surface water of the outmost stations. The bluest water was found in these areas caused by the lowest chlorophyll-a and lowest absorption of colored dissolved organic substances as well as low suspended matter concentrations (Hansen et al., 2014—in this issue). The surface water corresponded to oceanic water types OII to OIII according to Jerlov (1976) and was characterized by the highest spectral light penetration depths and euphotic depths.

#### 4.3. Pseudo-age

Mesoscale dynamics (eddies, filaments) can disturb the linear relation between age of upwelled water and distance to the coast along the transect. Based on water mass properties the age proxy “pseudo-age” was introduced to overcome as far as possible the impact of mesoscale dynamics on the simple 2-dimensional model of coastal upwelling. The succession of ecosystem components (nutrients, plankton, etc.) depends on aging of the upwelled water. Usually, the age of upwelled water is parameterized by the coastal distance, assuming a monotonic offshore transport in the surface layer. This parameterization is largely biased by mesoscale dynamics. In contrast, the PA approach uses time dependent water mass properties instead of the coastal distance to derive a proxy for the age of upwelled water at the surface. Nevertheless, there is an impact of mesoscale dynamics on the PA approach. Once upwelled, the water is not completely isolated on its way from the coast towards the open ocean. Mixing at the base of the surface mixed layer and at fronts to the ambient oceanic water causes an entrainment into the upwelling water. This entrainment can be a source or sink for any of the water mass properties, and thus potentially affect the estimation of pseudo-age. However, near the coast the effect of mesoscale dynamics on the PA is assumed to be low, since the intensity of mesoscale dynamics is weak and mixing with ambient water is low. Here the PA approach is based on oxygen concentration and temperature. Both parameters are mainly controlled by the surface flux and in the case of oxygen by the primary production too. Further offshore only the relation between temperature and salinity is used for the PA calculation. Mesoscale dynamics accelerates the change of water mass properties by mixing, but will not alter the temporal order. The main purpose for using the PA is to order the particular measurements with respect to time. The absolute value of PA is only a very rough estimate of the real age of the upwelled water, and of course to a certain extent affected by mesoscale dynamics.

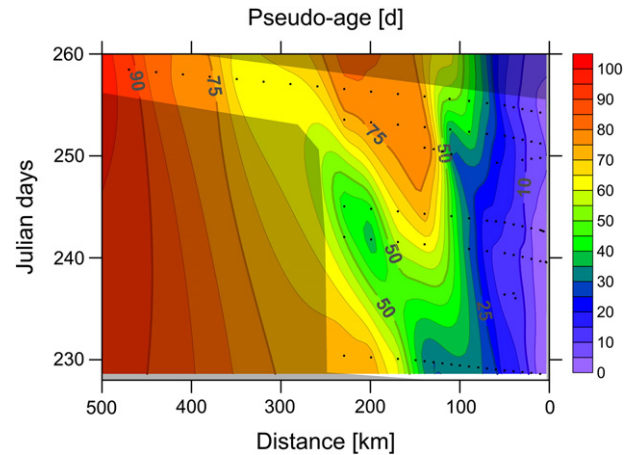


Fig. 16. Hovmöller plot of ‘pseudo-age’ along the SUCCESSION transect, based on vertically averaged CTD data from the surface to 20 m depth. Black dots indicate the positions of CTD casts.

Fig. 16 shows the distribution of PA for the time of the expedition. Not surprisingly it depicts the similar structure than temperature and salinity and highlights the impact of the filament structure on the age distribution along the transect. Within the first 100 to 150 km from the coast the PA increases with distance from the coast. At greater distances the mesoscale dynamics alters the PA distribution at some locations. Thus, the use of PA instead of coastal distance for the description of plankton succession may deliver more reasonable results.

Additionally, the PA provides a raw estimate for primary production in the coastal belt. The PA depends on the first aging period from the heat and oxygen fluxes into the surface water. Both fluxes are available from the model results. The oxygen flux directly at the coast is about  $2 \mu\text{mol m}^{-2} \text{s}^{-1}$  and decreases linearly towards the open ocean. Its sign changes at a distance of approximately 40 km offshore. The observed increase in oxygen concentration within a distance of 40 km from the coast amounts to  $133.9 \mu\text{M}$ . The time required for this input amounts to 38 days, assuming a 25 m thick mixed layer and a mean oxygen flux of  $1 \mu\text{mol m}^{-2} \text{s}^{-1}$ . Simultaneously to the oxygen flux, a temperature increase of 1.35 K is observed. From a mean net heat flux of  $125 \text{ W m}^{-2}$  and again for a 25 m thick mixed layer, the time for the temperature increase results in 13.4 days. This is roughly three times faster than the time for the corresponding oxygen uptake. At the inner shelf the numerical model gives an Ekman offshore velocity of 0.03 to  $0.04 \text{ m s}^{-1}$  during the cruise period. Accordingly, the 40 km distance is traveled within 13 days. This compares well with the estimate from the heat flux. The difference to the estimate based on the oxygen flux can be explained by primary production as additional oxygen source. To balance the oxygen deficit, the primary production must contribute approximately  $88 \mu\text{M}$  oxygen during the first aging phase. This oxygen amount is equivalent to a biomass production of about  $2300 \text{ mg m}^{-3}$  dry mass and compares well with the observations of primary production by Wasmund et al. (2005).

Another example for the successful application of PA approach is the investigation of phosphorus transformation along the “SUCCESSION” transect by Nausch and Nausch, 2014—in this issue.

## 5. Conclusions

A combination of field observations, remote sensing data and numerical simulations was used to investigate the hydrographic and hydrochemical conditions on the northern Namibian shelf during the seasonal maximum of coastal upwelling. In situ measurements were carried out along a 500 km long transect across the shelf at 20°S to 22°S. Remote sensing data supplied information about the spatio-temporal patterns of wind field, SST and chlorophyll-a distribution.

The numerical simulations were used to gather a comprehensive picture of the system in space and time and to obtain the impact of lateral advection on the 2D observations along the transect. A major attempt was the analysis of local wind forcing and its impact on the hydrographic and hydrochemical distributions in the upwelling area.

The main conclusions of the study are as follows:

- The upwelling season in 2011 was a “normal” year with upwelling intensity close to the climatological mean. This was proved against a climatology of wind forcing and with a time series of SST derived from remote sensing data. Hence, the hydrographic conditions that met during the cruise can be considered as representative or “typical” for the season.
- The supply of nutrient rich central water to the euphotic layer depends on coastal and wind stress curl driven upwelling. Both mechanisms act on different spatial scales and cause a horizontal zonation of the system. Three zones can be distinguished: 1) the coastal zone (0–50 km offshore) with coastal upwelling and high vertical velocities, 2) the wind stress curl driven upwelling zone (50–350 km offshore), characterized by slow entrainment of central water into the base of the surface layer, and 3) the oceanic region (>350 km distance to the coast), where no upwelling was observed.
- The hydrographic and hydrochemical conditions that met at the transect carry the signature of different source water masses, mostly with northern origin (SACW) and also influenced by ESACW at the oceanic stations. Biogeochemical processes and the mesoscale dynamics modify locally the properties of the water masses on the Namibian shelf.
- The SUCCESSION experiment reveals the temporal succession of the various ecosystem components in an offshore drifting water body after upwelling at the coast. The mesoscale dynamics cause disturbances in the strait correlation between age of upwelled water and the distance to the coast. The introduction of an age proxy (pseudo-age), based on the water mass properties and heat and oxygen fluxes through the surface, was successfully applied to reorder the observations along the SUCCESSION transect. Although, the local variability of the surface fluxes, mixing and mesoscale dynamics has an impact on the absolute value of PA, its temporal order is not influenced.
- The simulation results have shown that the advection in the surface layer is dominated by the alongshore current component. However, since the conditions at the coast were very similar along the northern Namibian shelf, a 2-dimensional conceptual model can be applied to describe the cross shelf dynamics.
- The comparison between observations and simulation results reveals akin distribution patterns in the upper layer. Thus, the sampling interval of the in situ observations at the transect seems to be sufficient to resolve the substantial patterns and processes in the investigation area.
- Although the simulated cross-shelf pattern of hydrographic and ecosystem variables compares generally with that found in the field measurements, there are significant differences especially in the near shore oxygen and chlorophyll distributions.

## Acknowledgment

We thank the Deutsche Forschungsgemeinschaft (DFG) for funding and support of the RV Merian cruises ABIMIX (MSM18/4) and SUCCESSION (MSM18/5). The assistance by the captain and crew of the RV Merian is much appreciated. Special thanks to Toralf Heene and Sebastian Beyer for their assistance during both data collection and analysis. The authors also wish to acknowledge the use of the Ferret program for analysis and graphics in this paper. Ferret is a product of NOAA's Pacific Marine Environmental Laboratory. (Information is available at <http://ferret.pmel.noaa.gov/Ferret/>.)

## References

- Albert, A., Echevin, V., Lévy, M., Aumont, O., 2010. Impact of nearshore wind stress curl on coastal circulation and primary productivity in the Peru upwelling system. *J. Geophys. Res.* 115 (C12), C12033. <http://dx.doi.org/10.1029/2010JC006569>.
- Bakun, A., 1990. Global climate change and intensification of coastal ocean upwelling. *Science* 247 (4939), 198–201.
- Bakun, A., Nelson, C.S., 1991. The seasonal cycle of wind-stress curl in subtropical eastern boundary current regions. *J. Phys. Oceanogr.* 21, 1815–1834.
- Bakun, A., Field, D.B., Redondo-Rodriguez, A., Weeks, S.J., 2010. Greenhouse gas, upwelling-favorable winds, and the future of coastal ocean upwelling ecosystems. *Glob. Chang. Biol.* 16, 1213–1228. <http://dx.doi.org/10.1111/j.1365-2486.2009.02094.x>.
- Bentamy, A., Fillon, D.C., 2011. Gridded surface wind fields from Metop/ASCAT measurements. *Int. J. Remote Sens.* 33, 1729–1754.
- Bentamy, A., Croize-Fillon, D., Perigaud, C., 2008. Characterization of ASCAT measurements based on buoy and QuikSCAT wind vector observations. *Ocean Sci.* 4, 265–274.
- Bentamy, A., Grodsky, S.A., Carton, J.A., Croizé-Fillon, D., Chapron, B., 2012. Matching ASCAT and QuikSCAT winds. *J. Geophys. Res.* 117 (C2), C02011. <http://dx.doi.org/10.1029/2011JC007479>.
- Bopp, L., Kohfeld, K.E., Le Quééré, C., 2003. Dust impact on marine biota and atmospheric CO<sub>2</sub> during glacial periods. *Paleoceanography* 18 (2), 1046. <http://dx.doi.org/10.1029/2002PA000810>.
- Carr, M.-E., 2002. Estimation of potential productivity in eastern boundary currents using remote sensing. *Deep-Sea Res.* II 49, 59–80.
- Carr, M.-E., Kearns, E.J., 2003. Production regimes in four eastern boundary current systems. *Deep-Sea Res.* II 50, 3199–3221.
- Charney, J.G., 1955. The generation of oceanic currents by wind. *J. Mar. Res.* 14, 477–498.
- Chavez, F.P., Messié, M., 2009. A comparison of eastern boundary upwelling ecosystems. *Prog. Oceanogr.* 83, 80–96.
- Cury, P., Shannon, L., 2004. Regime shifts in upwelling ecosystems: observed changes and possible mechanisms in the northern and southern Benguela. *Prog. Oceanogr.* 60, 223–243.
- Dogliotti, A.I., Schloss, I.R., Almandoz, G.O., Gagliardini, D.A., 2009. Evaluation of SeaWiFS and MODIS chlorophyll-a products in the Argentinean Patagonian Continental Shelf (38S–55S). *Int. J. Remote Sens.* 30 (1), 251–273.
- Duncombe Rae, C.M., 2005. A demonstration of the hydrographic partition of the Benguela upwelling ecosystem at 26°40'S. *S. Afr. J. Mar. Sci.* 27 (3), 617–628.
- FAO, 2012. The State of World Fisheries and Aquaculture – 2012. FAO, Rome (230 pp.).
- Feldman, G.C., McClain, C.R., 2012. Ocean Color Web – NASA Goddard Space Flight Center. <http://oceancolor.gsfc.nasa.gov/> WWW Page.
- Fennel, W., 1999. Theory of the Benguela upwelling system. *J. Phys. Oceanogr.* 29, 177–190.
- Fennel, W., Lass, H.U., 1989. Analytical Theory of Forced Oceanic Waves. Akademie-Verlag, Berlin.
- Fennel, W., Lass, H.U., 2007. On the impact of wind curls on coastal currents. *J. Mar. Syst.* 68 (1), 128–142.
- Fennel, W., Junker, T., Schmidt, M., Mohrholz, V., 2012. Response of the Benguela upwelling system to spatial variations in the wind stress. *Cont. Shelf Res.* 45, 65–77.
- Grasshoff, K., Ehrhardt, M., Kremling, K., 1983. Methods of Seawater Analysis, 2nd edition. Verlag Chemie, Weinheim.
- Gruber, N., Lachkar, Z., Frenzel, H., Marchesiello, P., Münnich, M., McWilliams, J.C., Nagai, T., Plattner, G.-K., 2011. Eddy-induced reduction of biological production in eastern boundary upwelling systems. *Nat. Geosci.* 4, 787–792. <http://dx.doi.org/10.1038/ngeo1273>.
- Gutknecht, E., Dadou, I., Marchesiello, P., Cambon, G., Le Vu, B., Sudre, J., Garçon, V., Machu, E., Rixen, T., Kock, A., Flohr, A., Paulmier, A., Lavik, G., 2013. Nitrogen transfers off Walvis Bay: a 3-D coupled physical/biogeochemical modeling approach in the Namibian upwelling system. *Biogeosciences* 10, 4117–4135.
- Hagen, E., Feistel, R., Agenbag, J.J., Ohde, T., 2001. Seasonal and interannual changes in intense Benguela upwelling (1982–1999). *Oceanol. Acta* 24, 557–568.
- Hansen, A., Wasmund, N., Ohde, T., 2003. Succession of micro- and nanoplankton groups in ageing upwelled waters off Namibia. *J. Mar. Syst.* 140, 130–137 (in this volume).
- Hardman-Mountford, N.J., Richardson, A.J., Agenbag, J.J., Hagen, E., Nykjaer, L., Shillington, F.A., Villacastin, C., 2003. Ocean climate of the South East Atlantic observed from satellite data and wind models. *Prog. Oceanogr.* 59, 181–221.
- Herzfeld, M., Schmidt, M., Griffies, S.M., Liang, Z., 2011. Realistic test cases for limited area ocean modelling. *Ocean Model.* 37, 1–34.
- Houry, S., Dombrowsky, E., De Mey, P., Minster, J.F., 1987. Brunt-Väisälä frequency and Rossby radii in the South Atlantic. *J. Phys. Oceanogr.* 17 (10), 1619–1626.
- Ianson, D., Allen, S.E., 2002. A two-dimensional nitrogen and carbon flux model in a coastal upwelling region. *Global Biogeochem. Cycles* 16 (1). <http://dx.doi.org/10.1029/2001GB001451> (2002).
- Jerlov, N.G., 1976. Marine Optics. Elsevier, Amsterdam.
- Jin, X., Dong, C., Kurian, J., McWilliams, J.C., Chelton, D.B., Li, Z., 2009. SST–wind interaction in coastal upwelling: oceanic simulation with empirical coupling. *J. Phys. Oceanogr.* 39 (11), 2957–2970. <http://dx.doi.org/10.1175/2009JPO4205.1>.
- Kent, E.C., Taylor, P.K., Challenor, P.G., 1998. A comparison of ship- and scatterometer-derived wind speed data in open ocean and coastal areas. *Int. J. Remote Sens.* 19 (17), 3361–3381. <http://dx.doi.org/10.1080/014311698214046>.
- Kostianoy, A.G., Zatsepin, A.G., 1996. The West African coastal upwelling filaments and cross-frontal water exchange conditioned by them. *J. Mar. Syst.* 7 (N2–4), 349–359.
- Large, W.G., Pond, S., 1981. Open ocean momentum flux measurements in moderate to strong winds. *J. Phys. Oceanogr.* 11, 324–336.
- Lass, H.U., Mohrholz, V., 2008. On the interaction between the subtropical gyre and the subtropical cell on the shelf of the SE Atlantic. *J. Mar. Syst.* 74, 1–49.

- Mendonça, A., Martins, A., Figueiredo, M., Bashmachnikov, I., Couto, A., Lafon, V., Aristegui, J., 2010. Evaluation of ocean color and sea surface temperature sensors algorithms using in situ data: a case study of temporal and spatial variability on two northeast Atlantic seamounts. *J. Appl. Remote. Sens.* 4, 43506.
- Mohrholz, V., Heene, T., 2012. Action of nonlinear internal waves at the Namibian shelf. Ocean Science Meeting, February 20–24, 2012, Salt Lake City, USA.
- Mohrholz, V., Schmidt, M., Lutjeharms, J.R.E., 2001. The hydrography and dynamics of the Angola-Benguela frontal zone and environment in April 1999. *S. Afr. J. Mar. Sci.* 97, 199–208.
- Mohrholz, V., Bartholomae, C.H., van der Plas, A.K., Lass, H.U., 2008. The seasonal variability of the northern Benguela undercurrent and its relation to the oxygen budget on the shelf. *Cont. Shelf Res.* 28, 424–441.
- Muller, A.A., 2013. Cross-Shore Exchange in the Northern Benguela and the Related Role of Upwelling Filaments. PhD thesis University of Cape Town, South Africa.
- Muller, A.A., Mohrholz, V., Schmidt, M., 2013. The circulation dynamics associated with a northern Benguela upwelling filament during October 2010. *Cont. Shelf Res.* 63, 59–68. <http://dx.doi.org/10.1016/j.csr.2013.04.037>.
- Muller-Karger, F.E., Varela, R., Thunell, R., Luerssen, R., Hu, C., Walsh, J.J., 2005. The importance of continental margins in the global carbon cycle. *Geophys. Res. Lett.* 32, L01602. <http://dx.doi.org/10.1029/2004GL021346>.
- Nash, D.N., Kunze, E., Toole, J.M., Schmitt, R.W., 2004. Internal tide reflection and turbulent mixing on the continental slope. *J. Phys. Oceanogr.* 34, 1117–1134.
- Nausch, M., Nausch, G., 2004. Phosphorus speciation and transformation along transects in the Benguela upwelling region. *J. Mar. Syst.* 140, 111–122 (in this volume).
- Philander, S.G.H., Yoon, J.H., 1982. Eastern boundary currents and coastal upwelling. *J. Phys. Oceanogr.* 12 (8), 862–879.
- Pickett, M.H., Paduan, J.D., 2003. Ekman transport and pumping in the California Current based on the U.S. Navy's high-resolution atmospheric model (COAMPS). *J. Geophys. Res.* 108 (C10), 3327. <http://dx.doi.org/10.1029/2003JC001902>.
- Renault, L., Dewitte, B., Falvey, M., Garreaud, R., Echevin, V., Bonjean, F., 2009. Impact of atmospheric coastal jet off central Chile on sea surface temperature from satellite observations (2000–2007). *J. Geophys. Res.* 114 (C8), C08006. <http://dx.doi.org/10.1029/2008JC005083>.
- Risien, C.M., Chelton, D.B., 2008. A global climatology of surface wind and wind stress fields from eight years of QuikSCAT scatterometer data. *J. Phys. Oceanogr.* 38, 2379–2413.
- Rohde, K.H., Nehring, D., 1979. Ausgewählte Methoden zur Bestimmung von Inhaltsstoffen im Meer- und Brackwasser. *Geod. Geophys. Veröff. R IV* 27, 1–68.
- Rouault, M., Illig, S., Bartholomae, Ch., Reason, C.J.C., Bentamy, A., 2007. Propagation and origin of warm anomalies in the Angola Benguela upwelling system in 2001. *J. Mar. Syst.* 68 (3–4), 473–488.
- Rykaczewski, R.R., Checkley, D.M., 2008. Influence of ocean winds on the pelagic ecosystem in upwelling regions. *PNAS* 2008 (105), 1965–1970.
- Schmidt, M., Eggert, A., 2012. A regional 3D coupled ecosystem model of the Benguela upwelling system. *Mar. Sci. Rep.* 87, 1–69.
- Shannon, L.V., Boyd, A.J., Brundrit, G.B., Taunton-Clark, J., 1986. On the existence of an El Niño-type phenomenon in the Benguela system. *J. Mar. Res.* 44 (3), 495–520.
- Shannon, L.V., Agenbag, J.J., Buys, M.E.L., 1987. Large- and mesoscale features of the Angola-Benguela front. In: Payne, A.L.L., Gulland, J.A., Brink, K.H. (Eds.), *The Benguela and Comparable Ecosystems*. South African Journal of Marine Science, Cape Town, pp. 11–34.
- Veitch, J., Penven, P., Shillington, F., 2010. Modeling equilibrium dynamics of the Benguela current system. *J. Phys. Oceanogr.* 40 (9), 1942–1964. <http://dx.doi.org/10.1175/2010JPO4382.1>.
- Wasmund, N., Lass, H.U., Nausch, G., 2005. Distribution of nutrients, chlorophyll and phytoplankton primary production in relation to hydrographic structures bordering the Benguela-Angolan frontal region. *Afr. J. Mar. Sci.* 27 (1), 177–190.
- Yoshida, K., 1955. Coastal upwelling off the California coast. *Rec. Oceanogr. Works Jpn.* 2, 8–20.